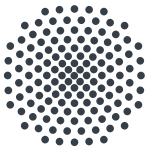

Universität Stuttgart
5. Physikalisches Institut

An accordion-type lattice: A tuneable dipole trap for ultracold gases

Master's thesis of
Carolin Dietrich

2nd November 2018

Examiner:	Prof. Dr. Tilman Pfau
Co-examiner:	Prof. Dr. Stephanie Barz

Universität Stuttgart
5. Physikalisches Institut
Pfaffenwaldring 57, 70569 Stuttgart

Ehrenwörtliche Erklärung

Hiermit versichere ich, gemäß der Prüfungsordnung der Universität Stuttgart für den Masterstudiengang Physik vom 31. Juli 2015,

- dass ich die vorliegende Arbeit selbstständig verfasst habe,
- dass ich keine anderen als die angegebenen Quellen benutzt und alle wörtlich oder sinngemäß aus anderen Werken übernommenen Aussagen als solche gekennzeichnet habe,
- dass diese Arbeit weder vollständig noch in wesentlichen Teilen Gegenstand eines anderen Prüfungsverfahrens gewesen ist,
- dass das elektronische Exemplar mit den anderen Exemplaren übereinstimmt.

Stuttgart, den 2. November 2018 Carolin Dietrich

Contents

1 Introduction

In 1926, Erwin Schrödinger published his famous equation, introducing the concept of the wavefunction [1]. Ever since, the electron wave function has been fundamental to understanding the properties of atoms, molecules and solid matter. The mean square of the wave function can be understood as the electron's probability density, thereby defining the shape of atomic orbitals. Although most textbooks concerning atomic physics have depicted representations of electron orbitals for decades, measurements that visualise these orbitals are fairly recent. The atoms' small size poses a significant challenge. The diameter of a single ground state atom is only a few Ångström, which is far smaller than optical wavelengths and is therefore outside the reach of measurement with an optical microscope.

In 2013 Stodolna et al. [2] were able to reconstruct an image of the wave function of a hydrogen atom by directly measuring the nodal structure of its Stark states using photoionisation microscopy. Orbitals of large molecules have also been measured using methods such as scanning tunneling microscopy [3] or photoemission spectroscopy [4].

A novel technique for wave function imaging proposed by Karpiuk et al. [5] circumvents the problem posed by the atom's small size by measuring the orbital of a Rydberg atom.

Rydberg atoms have an electron in a highly excited state, which results in a number of extraordinary and exaggerated properties. One of these exagerated properties is its orbital radius, which can be on the micron scale for a Rydberg state with a principle quantum number in the range of $n \approx 100$. Objects of the size of µm can be well resolved using currently established optical microscopy, however the orbital of a single electron cannot be measured directly. A contrast medium, that interacts with the electron and the light, is necessary.

The proposed contrast medium is a Bose-Einstein condensate (BEC). The interaction between the Rydberg electron and the surrounding ground state atoms in the BEC can be described with a scattering potential that causes the ground state atoms to experience an attractive force towards areas of high Rydberg electron probability. Thus the electron probability distribution is imprinted onto the density of the BEC. The density imprint can be visualised using phase contrast imaging.

The quality of the wave function imaging, in particular the contrast, is expected to improve by confining the ultracold atoms in a flat, quasi-2D trapping potential compared to a cigar shaped potential as is typical for magnetic traps [5].

The topic of this master thesis is the setup and characterisation of an accordion lattice that fulfills the technical requirements for wave function imaging. The working principle of the accordion lattice is the intersection of two equivalent laser beams at a variable angle. This results in an interference pattern consisting of bright layers. The spacing can be modified by varying the angle of intersection, thereby pressing the layers together and pulling them apart, similar to an accordion. Further expansion of the setup can include an active stabilisation with complete phase control.

The idea is to achieve a quasi 2D-layer of quantum gas by loading the atoms

into a single plane of the optical lattice at large spacing. The spacing can then be reduced until the desired confinement of the atoms is reached. This procedure avoids loading multiple layers of the lattice.

The accordion lattice presented in this thesis can achieve a lattice spacing between 3.5 µm and 35 µm.

The theoretical concept of wavefunction imaging which serves as the motivation to this work is covered in detail in chapter 3. In order to provide a basis of understanding , an overview of the properties and interactions of BECs and Rydberg-atoms is given in sections 3.1 and 3.2. Chapter 4 focusses on the theoretical concepts of optical dipole traps in general. It lists a number of various applications for ultracold atoms in lattices and explains the working principle of dipole traps. It also briefly covers heating mechanisms, that can cause the atoms to leave the trap, and introduces tunneling.

A description of the design and setup of the accordion lattice can be found in chapter 5. It includes characterisation measurements of the camera, which is a crucial part of the measurements detailed in chapter 6 and 7. Lastly chapter 9 contains a brief comparison between different types of quasi-2D dipole traps.

2 Zusammenfassung auf deutsch

Im Jahre 1926 veröffentlichte Erwin Schrödinger die Formel, die den Begriff der Wellenfunktion einführte und ihn weltberühmt machte [1]. Seitdem ist die Wellenfunktion von Elektronen fundamentaler Bestandteil für das Verständnis von Atomen, Molekülen und Festkörpern. Das Betragsquadrat der Wellenfunktion kann als die Wahrscheinlichkeitsdichte des Elektrons aufgefasst werden. Es definiert somit die Form atomarer Orbitale. Obwohl unzählige Physiklehrbücher bereits seit Jahrzehnten bildliche Darstellungen von Elektronenorbits enthalten, gibt es erst seit sehr kurzer Zeit erfolgreiche Messungen, die den Elektronenorbit visualieren. Aufgrund der äußerst kleinen Ausdehnung des Atoms, stellt seine Vermessung eine beträchtliche Herausforderung dar. Der Druchmesser eines einzelnen Grundzustandsatoms beträgt nur wenige Ångström, was deutlich kleiner ist als optische Wellenlängen. Deshalb die Abbildung des Atoms außerhalb der Möglichkeiten von bisherigen optischen Mikroskopen.

2013, fast ein Jahrhundert nach Schrödingers Veröffentlichung waren Stodolna et al. [2] in der Lage, ein Bild der Wellenfunktion eines Wasserstoffatoms zu rekonstruieren, indem sie direkte Messungen der Knotenstruktur von Stark -zuständen mit einem Photionisationsmikroskop durchführten. Es existieren auch andere Messmethoden für große molekulare Orbitale, wie beispielsweise Rastertunnelmikroskopie [3] oder Photoemissionsspektroskopie [4].

Eine neuartige Methode zur Abbildung von Wellenfunktionen, die das Problem der geringen atomaren Ausdehnung umgeht, wurde 2015 von Karpiuk et al. vorgeschlagen [5]. Es wurde die Vermessung von Rydbergorbitalen vorgeschlagen.

Rydbergatome haben ein Elektron in einem hoch angeregten Zustand. Dies führt zu einer Reihe außergewöhlicher und extremer Eigenschaften. Eine dieser Eigenschaften ist the enorme Größe des Orbitalradius, welche für einen Rydbergzustand mit einer Hauptquantunzahl $n \approx 100$ im Bereich von µm liegt. Objekte dieser Größe können mit den bereits etablierten optischen Mikroskopiemethoden direkt abgebildet werden, jedoch gilt dies nicht ohne Weiteres für ein einzelnes Elektron. Ein Kontrastmedium wird benötigt, das sowohl mit dem Elektron als auch mit dem Licht interagiert.

Die Kontrastmedium, das von Karpiuk et al. vorgeschlagen wurde, ist ein Bose-Einstein-Kondensat (BEK). Die Wechselwirkung zwischen dem Rydbergatom und den Grundzustandsatomen im BEK kann durch ein Streupotential beschrieben werden, das eine Kraft auf die Grundzustandsatome ausübt, sodass sie zu Regionen mit hoher Aufenthaltswahrscheinlichkeit des Rydbergelektron hingezogen werden. Somit kann die Wahrscheinlichkeitsdichte des Elektrons auf die Dichte des BEK geprägt werden. Die Aufprägung auf die Dichteverteilung kann mittels einer Phasenkonstrastabbildung visualisiert werden.

Es wird erwartet, dass die Qualität der Abibildung der Wellenfunktion, insbesondere der Kontrast, zunimmt, wenn die ultrakalten Atome des BEKs in einem quasi zwei-dimensionalen Fallenpotential gefangen sind, im Vergleich zu Abbildungen, die mit einem BEK aufgenommen werden, die sich in einem zylindrischen, dreidimensionalen Fallenpotential befinden [5].

Das Thema dieser Masterarbeit ist der Aufbau und die Charakterisierung eines „Accordion Lattice“, eines komprimierbaren Gitters, das die technischen Anforderungen für die Abbildung von Wellenfunktionen erfüllt. Das Prinzip des Akkordeon Gitters ist die Kreuzung zweier äquivalenter Strahlen unter einem veränderlichen Winkel. Dies führt zu einem Interferenzmuster mit hellen und dunklen Schichten. Der Abstand zwischen den Schichten kann durch Veränderung des Kreuzungswinkels variiert werden. Dadurch werden die einzelnen Schichten des Gitters zusammengepresst oder auseinander gezogen, ähnlich dem Zusammendrücken und Auseinanderziehen eines Akkordeons. Eine Erweiterung des Aufbaus kann eine Regelung der Phase, sowie eine aktive Phasenstabilisierung enthalten.

Die Idee zur Erzeugung einer quasi-zwei-dimensionalen Falle mit dem Accordion Lattice beruht darauf, dass die Atom bei großem Gitterabstand in eine einzelne Schicht des Interferenzmusters geladen werden können, woraufhin der Gitter -abstand komprimiert werden kann, bis die gewünschten Einschlussparameter erreicht sind. Dieses Verfahren vermeidet das Laden mehrerer Schichten des Gitters mit Atomen.

Das Accordion Lattice, welches in dieser Arbeit vorgestellt wird, kann Gitterabstände im Bereich von 3.5 µm bis 35 µm realisieren.

Eine detailierte theoretische Beschreibung des Wellenfunktionsabbildung, welche die Motivation für diese Arbeit darstellt, befindet sich in Kapitel 3. Um ein Grundverständnis der darin enthaltenen Prinzipien zu gewährleisten, werden zunächst in Abschnitt 3.1 und 3.2 die Eigenschaften von BEKs und Rydbergatomen, sowie ihrer Wechselwirkung dargelegt. Kapitel 4 behandelt die Funktionsweise von optischen Dipolefallen im Allgemeinen. Es führt eine Reihe von Anwendungen kalter atomarer Gase in Gitterexperimenten auf und erklärt die theoretischen Grundlagen zur Dipolkraft und den Fallenpotentialen. Das Kapitel enthält auch einen Abschnitt zu Heizmechanismen in Dipolfallen, die dazu führen können, dass die Atome die Falle verlassen. Außerdem wird Tunneln von Atomen von einem Potentialtopf zum nächsten angesprochen.

Eine Beschreibung des Aufbaus sowie eine schematische Darstellung des Accordion Lattice befinden sich in Kapitel 5. Es beinhaltet Charakterisierungsmessungen der verwendeten Kamera, da sie wesentlicher Bestandteil der Messungen in den darauffolgenden Kapiteln 6 und 7 darstellt. Zuletzt wird in Kapitel 9 ein Vergleich des Accordion Lattice mit alternativen quasi-zwei-dimensionalen Fallen gezogen.

3 Wave function imaging

The following chapter serves as an introduction to the relevant physical concepts by providing the necessary basic understanding needed for the scope of this thesis: a anccordion lattice for the purpose of directly imaging a Rydberg electron orbital. Wave function imaging could allow us to optically measure the atomic orbital of a Rydberg atom using an ultracold quantum gas as a contrast medium. Therefore an overview of the relevant properties of Bose-einstein condensates (BECs) and of Rydberg atoms in general is provided, before the working principles of wave function imaging are explained in theory and the possible experimental realisation is outlined.

3.1 Bose-Einstein-Condensate (BEC)

Imagine cooling down a cloud of identical particles with a mass of m. The thermal de-Broglie wavelength λ_{dB} increases

$$\lambda_{\mathrm{dB}} = \hbar\sqrt{\frac{2\pi}{mk_{\mathrm{B}}T}}, \tag{1}$$

with decreasing distance between the particles, until both lengths are of similar size, so that

$$n\lambda_{\mathrm{dB}}^3 > 1, \tag{2}$$

where n is the particle density. A critical phase space density is then reached and the system undergoes a phase transition called Bose-Einstein-condensation, named after S. A. Bose and A. Einstein who predicted this phenomenon in 1924 [7, 8].

For identical, non-interacting particles a critical temperature T_{crit} can be attributed to the phase transition at

$$T_{\mathrm{crit}} = \frac{2\pi\hbar^2}{mk_{\mathrm{B}}}\left(\frac{n}{2,612}\right)^{2/3} \text{[9]}. \tag{3}$$

When the temperature drops beneath the critical temperature, the atoms condensate into a macroscopically populated ground state while a fraction of the particles remains thermally excited. The wave functions of the individual atoms begin to overlap and the behaviour of the cloud can no longer be described with classical means. Due to constructive interference of the wave functions, a single macroscopic wave function can be attributed to the atoms residing within the collective ground state. The amount of particles in the ground state depends on the temperature. In the case of an ideal, non-interacting BEC with N particles in a three-dimensional harmonic potential the fraction of particles in the ground state equals

$$\frac{N_0}{N} = 1 - \left(\frac{T}{T_{\mathrm{crit}}}\right)^3 \text{[9]}. \tag{4}$$

According to equation (4) all particles are in the ground state at $T = 0$ K. This is not true for experimentally realised BECs where the particles interact with each other. This effect is called quantum depletion. Weakly interacting particles can be described by assuming finite pressure and a chemical potential even at $T = 0$ K [9].

3.1.1 Gross-Pitaevskii equation (GPE)

Within the context of the Bogoliubov theory the behaviour of a BEC of weakly interacting atoms can be modelled with the Gross-Pitaeskii-Equation (GPE). Using quantum field theory the GPE can be derived from a many-body Hamiltonian $\hat{H}$ in second quantisation

$$\begin{aligned}\hat{H} = &\int \mathrm{d}^3 r \hat{\Psi}^\dagger(\boldsymbol{r}) \left(-\frac{\hbar^2}{2m}\nabla^2 + V_{\mathrm{ext}}(\boldsymbol{r}) \right) \hat{\Psi}(\boldsymbol{r}) \\ &+ \frac{1}{2} \iint \mathrm{d}^3 r \mathrm{d}^3 r' \hat{\Psi}^\dagger(\boldsymbol{r}) \hat{\Psi}^\dagger(\boldsymbol{r'}) U(\boldsymbol{r}-\boldsymbol{r'}) \hat{\Psi}(\boldsymbol{r'}) \hat{\Psi}(\boldsymbol{r}),\end{aligned} \tag{5}$$

where the first integral contains terms describing the kinetic energy in the condensate, and a potential $V_{\mathrm{ext}}(\boldsymbol{r})$, provided by external fields, for example by an optical or magnetic trap [10]. The second integral describes the interaction between the particles with an interaction potential $U(\boldsymbol{r}-\boldsymbol{r'})$. $\hat{\Psi}(\boldsymbol{r})$ and $\hat{\Psi}^\dagger(\boldsymbol{r})$ are bosonic field operators. Due to symmetry they fulfill the following commutation relations:

$$\begin{aligned}[\hat{\Psi}(\boldsymbol{r}), \hat{\Psi}^\dagger(\boldsymbol{r'})] &= \delta(\boldsymbol{r}-\boldsymbol{r'}), \\ [\hat{\Psi}(\boldsymbol{r}), \hat{\Psi}(\boldsymbol{r'})] &= 0, \\ [\hat{\Psi}^\dagger(\boldsymbol{r}), \hat{\Psi}^\dagger(\boldsymbol{r'})] &= 0.\end{aligned} \tag{6}$$

The time-evolution of the field operators in the Heisenberg picture behaves according to

$$i\hbar \frac{\partial}{\partial t} \hat{\Psi}(\boldsymbol{r}, t) = [\hat{\Psi}(\boldsymbol{r}), \hat{H}]. \tag{7}$$

Together with the commutation relations (6), equation (7) can be written as

$$\begin{aligned}i\hbar \frac{\partial}{\partial t} \hat{\Psi}(\boldsymbol{r}, t) = &\left(-\frac{\hbar^2}{2m}\nabla^2 + V_{\mathrm{ext}}(\boldsymbol{r}) \right) \hat{\Psi}(\boldsymbol{r}) \\ &+ \int \mathrm{d}^3 r' \hat{\Psi}^\dagger(\boldsymbol{r}) \hat{\Psi}^\dagger(\boldsymbol{r'}) U(\boldsymbol{r}-\boldsymbol{r'}) \hat{\Psi}(\boldsymbol{r'}) \hat{\Psi}(\boldsymbol{r}).\end{aligned} \tag{8}$$

It is then assumed, that the density distribution can be described as a scalar field with small fluctuations. Hence the field operator can be changed to

$$\hat{\Psi}(\boldsymbol{r}) = \langle \hat{\Psi}(\boldsymbol{r}) \rangle + \delta\hat{\Psi}(\boldsymbol{r}) \tag{9}$$

with $\langle \hat{\Psi}(\boldsymbol{r}) \rangle$ as an order parameter [10]. We consider a BEC with a temperature well below the critical temperature (3). The majority of particles are in the ground state. This allows us to use the mean-field-approximation, neglecting the fluctuations and replacing $\langle \hat{\Psi}(\boldsymbol{r}) \rangle$ with a scalar order parameter [9]

$$\psi(\boldsymbol{r}, t) = \sqrt{N_0}\psi_0(\boldsymbol{r}, t). \tag{10}$$

$N_0 \gg 1$ is the number of particles in the ground state.

The interaction between two atoms can be described as a binary collision [10] and the interaction potential can therefore be written as

$$U(\boldsymbol{r} - \boldsymbol{r}') = g\delta(\boldsymbol{r} - \boldsymbol{r}'), \tag{11}$$

which corresponds to a contact interaction with a coupling constant g. The couplin constandt is defined as

$$g = \frac{4\pi\hbar^2 a_\mathrm{s}}{m} \tag{12}$$

with the scattering length a_s of the particles [10]. In general, the scattering can also include higher partial waves, however for sufficiently low temperatures only s-wave scattering is taken into account [9].

Plugging the interaction potential into equation (8) gives us the time-dependent Gross-Pitaevskii equation (GPE)

$$i\hbar\frac{\partial}{\partial t}\psi(\boldsymbol{r}, t) = \left[-\frac{\hbar^2}{2m}\nabla^2 + V_\mathrm{ext}(\boldsymbol{r}) + g|\psi(\boldsymbol{r}, t)|^2\right]\psi(\boldsymbol{r}, t), \tag{13}$$

which corresponds to a non-linear Schrödinger equation for the condensate wave function. It describes the collective dynamics only of the particles in the macroscopically populated state, particles in other states are neglected [10]. $\psi(\boldsymbol{r}, t)$ refers to the condensate wave function dependent on time t and position $\boldsymbol{r}$.

$$|\psi(\boldsymbol{r}, t)|^2 = N_0|\psi_0(\boldsymbol{r}, t)|^2 \tag{14}$$

can be considered the density distribution of the BEC [9].

This shows one of the main advantages of experiments using a BEC: it displays uniform behaviour which can be modelled with a single collective wave function.

3.1.2 Experimental realisation

Although the theoretical prediction of BEC exists since 1924 [7, 8], it was several decades before a BEC could be realised in 1995 by two groups, the group of E. Cornell and C. Wieman in Colarodo using Rubidium [11] and the group of W. Ketterle at MIT using Sodium [12].

The reason why there is such a large gap in time between theory and experiment is that the necessary cooling methods hadn't been developped yet, as well as the lasers, which are vital for the application of those methods [13]. This section gives a brief overview of some of those cooling techniques.

The first requirement for creating a BEC is a cloud of atoms enclosed by a vacuum. The vacuum is necessary in order to avoid collisions with background gas and heating [14]. The atoms have to be of a single species, as the phase transition relies on the symmetrical properties of the bosons and their indistinguishability [15]. However, subsequent mixing of condensates in order to create a dual-species BEC is possible [16]. Atomic clouds are often produced by heating an atom source. The atoms in the resulting cloud are too fast and hot to be condensed into a BEC. They have to be slowed down and pre-cooled first. One method of achieving this is the Zeeman slower [17].

In a Zeeman slower the hot atoms travel through a cylinder through which a laser beam is directed, so that the beam is counter-propagating the atoms' motion along the cylinder. The laser beam is resonant with the atoms, so that they absorb the incoming photons and spontaneously emit them in a random direction, thus resulting in a force in direction of the beam, which slows them down. In order to compensate the Doppler shift due to the reduced velocity, a magnetic field gradient is applied along the tube. This causes a Zeeman shift which is dependent on the position of the atoms along the tube. The Zeeman shift compensates the Doppler shift and the laser remains in resonance with the atoms. The atoms as hot as 300 K can be cooled down to a few Kelvin using this method [17].

Another method that uses the spontaneous light force is Doppler cooling, also referred to as optical molasses. It uses counter-propagating beam pairs with a red detuning relative to the atoms' resonance to cool down atoms down to the Doppler limit, which is defined by the natural linewidth Γ of the atomic transition

$$T_{\text{Doppler}} = \frac{\hbar\Gamma}{2k_{\text{B}}}. \tag{15}$$

Temperatures as low as tens of µK can be reached [18]. While Doppler cooling slows the atoms down, it doesn't trap them, the atoms will eventually be lost.

The magneto-optical trap (MOT) on the other hand combines trapping and cooling of atoms. The coils around the trap are in anti-helmholtz configuration leading to a position-dependent Zeeman shift. The cloud of atoms trapped inside the (MOT) is cooled down using Doppler cooling. The counter-propagating beams have circular polarisation. This method of cooling is also limited by the Doppler limit. For Alkali atoms such as Rubidium a minimal temperature on the order of 100 µK can be reached [14], which is still orders of magnitude above the critical temperature, but the atoms are now cold enough to be transferred into a different trap for further cooling.

This trap can be a magnetic quadrupol trap. The atoms are cooled down using radio-frequency (RF) evaporation, where the hottest atoms are selectively removed from the trapping potential, until the cloud condensates into a BEC. The critical temperature depends on the density of the cloud and on the atomic mass of the particles. To give an example, using equation (3) as an approximation, a cloud of Rubidium 87 with a density of n =5 x 10^{13} cm^{-3} condensates at around 250 nK, which is within a realistic range compared to experimental data [14].

Once the atoms have been condensed into a BEC, they can be used in a variety of experiments such as for instance interferrometry or gyroscopes [19], dipolar BECs are very sensitive to magnetic fields [15] and could therefore be used as sensors.

The BEC is also an essential component for wave function imaging. To be able to image orbital of a Rydberg atom, the BEC serves as a contrast medium. The properties of the Rydberg atom, which is the second indispensable component for the wave function imaging, are described in the following section.

3.2 Rydberg atoms

Atoms that have a single electron in a highly excited state are called Rydberg atoms. The excited electron can be referred to as Rydberg electron.

To give an or example, principle quantum numbers of $n \approx 300$ have been achieved for Strontium [20], while interstellar Hydrogen can reach $n \approx 800$ [21]. The high principle quantum number dominates many physical properties of Rydberg atoms, exaggerating the values of these properties.

Rydberg atoms are extremely sensitive with respect to external electric fields, which means they interact strongly with their environment. Their extreme properties make them fascinating objects for research. For example, they act as very sensitive microwave resonators, which makes them excellent agents for probing and measuring small fields [22]. Due to strong long-range interactions between Rydberg atoms, they could be used for quantum simulations [23], or quantum information processing [24, 25, 26]. They have relevance in the area of ultracold plasma physics, because they are easily ionised by collisions which can lead to plasma formation [27, 28]. Rydberg atoms have also been proposed as single photon sources [29].

One of the extreme properties of Rydberg atoms is their size. In contrast to ground state atoms, which have a radius on the scale of a few Ångström, a Rydberg atom that is excited to $n \approx 100$ can have a radius on the micron scale [30]. Its orbital is large enough to be optically resolved, which opens the possibility of direct, optical measurements of a single atomic orbital [5]. In order to achieve the imaging of a Rydberg orbital a contrast medium has to be introduced that interacts with the Rydberg electron and the light. In our case this contrast medium is a BEC.

The relevant properties of Rydberg atoms that are necessary for understanding the concept of wave function imaging are explained in the following sections. All equations stated in this chapter about Rydberg atoms are given in atomic units.

3.2.1 Energy levels of a Rydberg atom

The energy level a hydrogen atom without any external fields is defined as

$$E_n = E_{\mathrm{Ryd}} \frac{1}{n^2} \tag{16}$$

with $E_{\mathrm{Ryd}} = 13.6$ eV being the Rydberg energy. Equation (16) depends only on the principle quantum number n, which means that the energy levels are degenerate with respect to the angular momentum l or spin s. Without an external magnetic field there is no finestructure in the hydrogen model.

The energy levels of alkali atoms and Rydberg atoms (excluding hydrogen) however, are described with a quantum defect $\delta_{n,l,j}$, that lifts this degeneracy

$$E = E_{\mathrm{Ryd}} \frac{Z^2}{(n - \delta_{n,l,j})^2} = E_{\mathrm{Ryd}} \frac{Z^2}{(n^*)^2} \tag{17}$$

and includes the nucleus charge Z. Equation (17) is still very similar to equation (16) of the Bohr-model of hydrogen. While the valence electron has been highly excited the remaining electrons shield the core's positive charge. The Rydberg electron can polarise the core electrons anisotropically and this leads to the

quantum defect which depends on n, the orbital angular momentum l and total angular momentum j. This effect is most pronounced for low-l states. The defect becomes smaller with increasing angular momentum and can be neglected after $l > 4$ [31, 32].

The defect originates from the Rydberg electrons interaction with the core. Electrons with higher angular momentum l are less likely to be found near the core than electron with low l. Therefore the defect is only relevant at low l [30]. It also lifts the degeneracy of the finestructure. Therefore Rydberg atoms can be excited into well- defined quantum states, such as s-, p- or d-states for example [5].

3.2.2 Scaling laws

Alkali atoms are often used for Rydberg excitation in the context of ultracold gases, because they have only one electron in their outermost shell and are easily cooled using methods of laser cooling.

Similar to alkali atoms with its single excited electron and the core which is shielded by the remaining non-excited electrons, many aspects of the behaviour of Rydberg atoms can be modelled with a hydrogen-like model in combination with central-field approximation (CFA) and quantum-defect theory [30].

In particular those physical properties, which are dominated by the effective principle quantum number n^* become extreme in Rydberg atoms, e. g. a ^{87}Rb atom excited to $n = 100$ has an orbital radius of about one micron, which is about four orders of magnitude larger a ground state atom of a few Ångström. A few examples of scaling are given in table 1.

Property:	Scales with
Orbital radius:	n^{*2}
Binding energy:	n^{*-2}
Radiative lifetime:	n^{*3}
Dipole moment:	n^{*2}
Polarisability:	n^{*7}
Van-der-Waals coefficient:	n^{+11}

Table 1: Properties of Rydberg atoms and their scaling with the effictive principle quantum number n^* [30]

3.2.3 Rydberg-electron wave function

The wave function of the Rydberg electron is defined by the Schrödinger equation

$$\left[-\frac{1}{2\mu}\nabla^2 + V(r)\right]\psi(r,\theta,\phi) = E\psi(r,\theta,\phi). \tag{18}$$

It contains the reduced electron mass μ and the core potential $V(r)$ and $\psi(r,\theta,\phi)$ is the Rydberg electron function. Assuming $V(r)$ has spherical symmetry and therefore no angular dependence, the Schrödinger equation (18) can be rewritten

in spherical coordinates

$$\left[-\frac{1}{2\mu r}\frac{\mathrm{d}^2}{\mathrm{d}r^2}r + \frac{\hat{L}^2}{2\mu r^2} + V(r)\right]\psi(r,\theta,\phi) = E\psi(r,\theta,\phi). \tag{19}$$

The wave function can thus be separated into a part with radial dependence $R(r)$

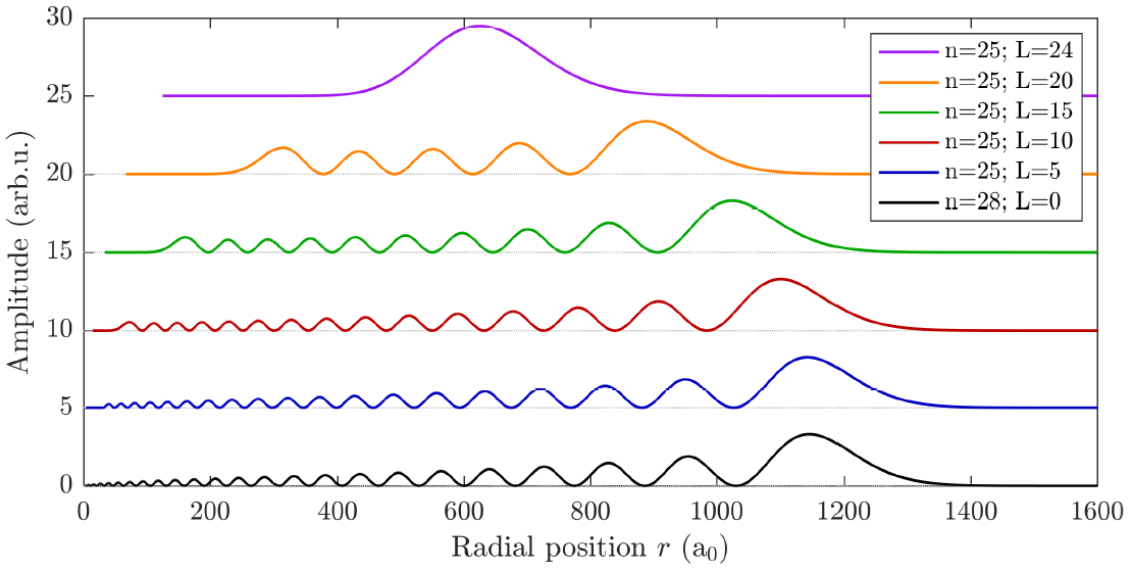

Figure 1: Absolute values of radial Rydberg electron wave functions with different angular momentum l. The lines are offset for easier comparison.[14]

and a part with angular dependence

$$\psi(r,\theta,\phi) = R(r)Y_l^m(\theta,\phi). \tag{20}$$

Laplace's spherical harmonics $Y_l^m(\theta,\phi)$ satisfy equation (19) and can be found in most textbooks concerning quantum physics such as [33]. So far the equations (18 - 20) are valid for hydrogen in general (including those excited to a Rydberg state). The radial part $R(r)$ of the electron wave function of alkali atoms and Rydberg atoms differs from the hydrogen model. It can be determined by solving the radial part of the Schrödinger equation

$$\left[-\frac{1}{2\mu r}\frac{\mathrm{d}^2}{\mathrm{d}r^2}r + \frac{l(l+1)}{2\mu r^2} + V_{\mathrm{mod}}\right]R(r) = E(r), \tag{21}$$

which contains a modified potential V_{mod} to account for the effective charge $Z_{\mathrm{eff}}(r)$, polarisability of the core and spin-orbit coupling

$$V_{\mathrm{mod}} = -\frac{Z_{\mathrm{eff}}(r)}{r} + V_{\mathrm{pol}} + V_{\mathrm{so}}. \tag{22}$$

The electrons in the core shield the positive charge from the Rydberg electron resulting in a reduced effective charge Z_{eff}. The polarisation potential V_{pol} is defined as

$$V_{\mathrm{pol}} = -\frac{\alpha_c}{2r^4}(1 - e^{(r/r_c)^6}) \tag{23}$$

where α_c is the polarisability of the core and r_c is a cutoff radius below which the polarisability becomes unimportant [34].

The effect of the spin-orbit coupling V_{so} is approximated by

$$V_{\mathrm{so}} \approx \frac{\alpha_{\mathrm{FS}}^2}{4r^3} \left(j(j+1) - l(l+1) - s(s+1)\right) \tag{24}$$

with the fine-structure constant α_{FS} [35]. Equation (21) can be solved numerically for $R(r)$.

Figure 1 demonstrates that electrons with higher angular momentum l are less likely to be found near the core than electrons with low l. This limits the interaction of the Rydberg electron with the core, leading to the extremely long radiative lifetimes of the Rydberg states, especially of high-l states. Rydberg states have very long lifetimes compared to their less excited counterparts. While a state that has been excited by a few n has a lifetime of a nanoseconds, a Rydberg state can exist for many microseconds before spontaneously decaying [30].

3.2.4 Rydberg blockade

Another extraordinary property of Rydberg atoms is their long-range interaction. Mutual interaction between Rydberg atoms can be more than ten orders of magnitude stronger than those between ground state atoms [26]. When two Rydberg atoms are in close proximity, they induce a dipole moment in each other owing to their strong polarisability. This leads to induced dipole-dipole interaction, which can be described by a van-der-Waals potential

$$V_{\mathrm{vdW}} = \frac{C_6}{R^6} \tag{25}$$

with a van-der-Waals coefficient $C_6 \propto n^{11}$ and the distance R between the two atoms. This leads to a strong long-range interaction between Rydberg atoms.

Once an atom has been photo-excited to a Rydberg state, this interaction causes a shift of the Rydberg energy level of the surrounding atoms, even if they themselves remain in the ground state. If the shift is larger than the bandwidth γ_L of the excitation laser, then the wavelength is no longer sufficient to excite them to the Rydberg state and no additional Rydberg atom can be created within a certain blockade radius [36]

$$r_{\mathrm{B}} = \left(\frac{C_6}{\hbar\gamma_L}\right)^{\frac{1}{6}}. \tag{26}$$

Typically, the linewidth of the Rydberg level is smaller than γ_L and is therefore neglected in equation (26) [14].

This effect is called the Rydberg blockade. Depending on the angular momentum l of the Rydberg state the Rydberg blockade can be anisotropic [37].

If the atoms within the blockade volume are indistinguishable, it is impossible to determine exactly which atom has been excited to a Rydberg state, the excitation becomes delocalised. The reason for this is that the atoms within the range of the

Rydberg atom are in a state, which is a superposition of all permutation of possible states with one excitation

$$|E\rangle = \frac{1}{\sqrt{N}}(|e,g,g,...\rangle + |g,e,g,...\rangle + |g,g,e,...\rangle + ...). \tag{27}$$

The Rydberg blockade is an essential effect that is exploited e. g. in single photon sources [29].

3.2.5 Interaction between Rydberg atoms and ground state atoms

The interaction between the Rydberg atom and the ground state atoms can be discussed in terms of scattering theory. The following evaluation can be found in most standard textbooks, which include scattering theory [9, 38].

Scattering processes can be modelled with the Schrödinger equation

$$\left[-\frac{\nabla^2}{2\mu} + V(R)\right]\Psi(\boldsymbol{R}) = E\Psi(\boldsymbol{R}), \tag{28}$$

wherein μ is the reduced mass of the two scattering partners, $V(R)$ is the scattering potential, R is the distance between the particles. $\Psi(\boldsymbol{R})$ denotes the scattering wave function. The ansatz for the scattering wave function is

$$\Psi(R,\theta) = \sum_{\ell=0}^{\infty} \mathcal{R}_{k\ell}(R) Y_\ell^m(\theta,\varphi) \tag{29}$$

with a radial wave function $\mathcal{R}_{k\ell}(R)$, and the spherical harmonics $Y_\ell^m(\theta,\varphi)$. Due to symmetry reasons only $m_\ell = 0$ are relevant, which means that the spherical harmonics can be reduced to the Legendre polynominals $P_\ell^0(\cos\theta)$. Note that ℓ is the angular momentum of the scattering process and not of the angular momentum l of the Rydberg state. Using this ansatz (29) the Schrödinger equation can be rewritten as

$$\left[-\frac{1}{2\mu R}\frac{\mathrm{d}^2}{\mathrm{d}R^2} + \frac{\ell(\ell+1)}{2} + V(R)\right]\mathcal{R}_{k\ell}(R) = E\mathcal{R}_{k\ell}(R). \tag{30}$$

The ground state atoms' interaction with the Rydberg electron and the ionic core can be treated separately according to the Born-Oppenheimer approximation. Scattering processes between the Rydberg electron and the ground state atoms are from now on referred to as electron-atom scattering and scattering between atoms and the ionic Rydberg core are referred to as ion-atom scattering.

If the electron is sufficiently far away from the core, the interaction between the Rydberg electron and the core is very weak and the Rydberg electron can therefore be described as a quasi-free particle. In the case of interaction ranges which are small compared to the de Broglie wavelength of the electron, the interaction can be described as a contact interaction using the Fermi-pseudo potential [39] which is defined as

$$V_{\mathrm{pseudo}}(\boldsymbol{r}) = \frac{2\pi\hbar^2 a}{m_e}\delta(\boldsymbol{r}) \tag{31}$$

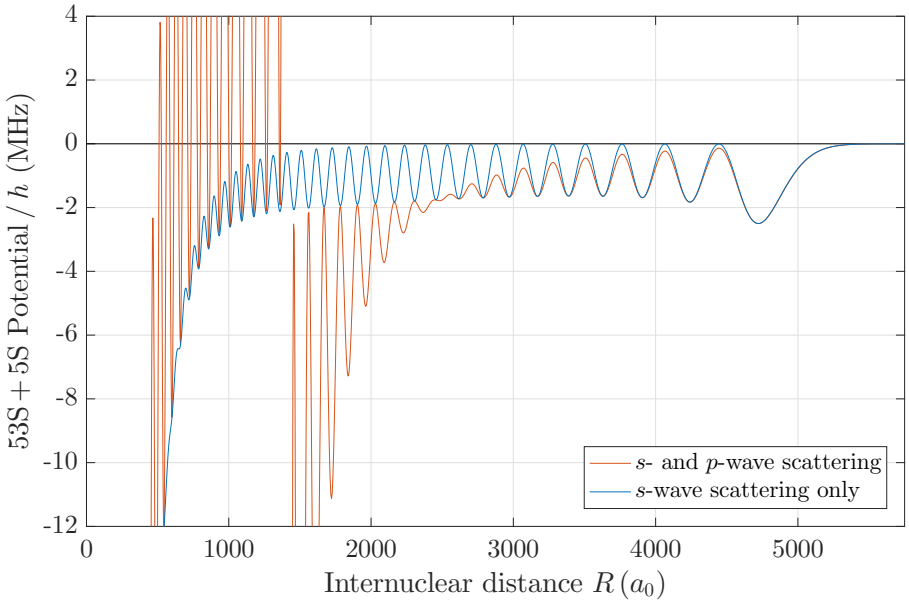

Figure 2: Interaction potential for an 53S Rydberg atom with 5S ground state atoms with and without taking into account p-wave scattering. The potential has been calculated for ^{87}Rb atoms. The effect of p-wave scattering is significant in a limited range of about 2000 a. u., for longer distances the p-wave scattering becomes negligible [40].

with the electron mass m_e and the scattering length a between the electron and the neutral atom. The interaction is described to be point-like. The scattering potential of the Rydberg electron with the atoms can be written as

$$V_{\mathrm{Ryd}}(\boldsymbol{R}) = \int V_{\mathrm{pseudo}}(\boldsymbol{r}-\boldsymbol{R})|\psi_{\mathrm{Ryd}}(\boldsymbol{r})|^2 \mathrm{d}^3r = \frac{2\pi\hbar^2 a}{m_e}|\psi_{\mathrm{Ryd}}(\boldsymbol{R})|^2. \tag{32}$$

$\psi_{\mathrm{Ryd}}(\boldsymbol{r})$ denotes the Rydberg electron wavefunction and $|\psi_{\mathrm{Ryd}}(\boldsymbol{r})|^2$ is the electron's density distribution. The scattering length a is the s-wave scattering length between a free electron and a neutral ground state atom. At low temperatures only the s-wave scattering is taken into account, however p-wave shape resonance can occur. The p-wave shape resonance only contributes in a limited range, which is demonstrated in figure 2.

The ion-atom scattering can be classically described using a polarisation potential

$$V_i(R) = -\frac{\alpha}{2R^4} = -\frac{C_4}{R^4}. \tag{33}$$

It is also referred to as C_4-potential and α is the ground state polarisability of the atoms. For ^{87}Rb the polarisability is $\alpha = 318.8$ a. u. [41]. The interaction range between a ^{87}Rb$^+$-ion and a ^{87}Rb-atom can be approximated to $R_i = \sqrt{m_{Rb}C_4} \approx 5025$ a. u..

Thus, for sufficiently high n, the ground state atoms interact with the ionic core only for very small internuclear distances. The Rydberg electron on the other hand interacts with any atom that enters it's orbital and therefore has a much larger

interaction range. In consequence the interaction with the core is only relevant for samples with high density and can be neglected under most experimental conditions.

The interaction of the Rydberg atom with its surrounding medium also influences its lifetime. Increasing the particle density leads to more collisions with other atoms which can result in decay or even ionisation of the Rydberg atom [42].

In an experiment the lifetime of the Rydbeg state limits the interaction time between the Rydberg electron and its environment. This is also true for wave function imaging, a technique that relies on the the interaction between a Rydberg atom and a BEC, which is discussed in the following section.

3.3 Microscopy of atomic orbitals

This chapter explains the theory behind wave function imaging, it is based on a proposal by Karpiuk et al.[5]. The idea is to optically measure the electronic orbital of a Rydberg atom. Advantages of using Rydberg atoms for wave function imaging are the size of the orbital and the prospect of achieving textbook like images e. g. of S- or D-orbitals.

Optically measuring the Rydberg elctron orbital requires a medium that interacts with the Rydberg electron and the imaging beam. A BEC fulfills this requirement and is therefore used as a medium. Properties of BECs and Rydberg atoms have been covered in previous sections and wave function imaging exploits the interaction between those two components.

Imagine a single Rydberg atom inside a BEC. As mentioned in section 3.2, Rydberg atoms interact strongly with their environment, in our case the surrounding ground state atoms, many of which are enclosed within the Rydberg electron's orbital.

The interaction with the Rydberg core can be neglected, thus only the Rydberg electron-atom scattering is taken into account. The effect of the Rydberg atom on the BEC can be modelled eit the scattering potential, which has already been introduced in chapter 3.2.5

$$V_{Ryd}(\boldsymbol{r}) = \frac{2\pi\hbar^2 a}{m_e}|\psi_{Ryd}(\boldsymbol{r})|^2. \tag{34}$$

The Rydberg electron is regarded as a quasi-free particle, so the interaction between the electron and the ground state atoms is reduced to the scattering length a. In the experiment at hand a is the triplet s-wave scattering length between a free electron and a ground state atom. Due to an external magnetic field, the spins of the ground state atoms and the Rydberg electron are parallel, in consequence the scattering is triplet scattering. For the case of ^{87}Rb the triplet scattering length is $a = -16.1$ a. u. [43]. The sample is prepared with parallel spins resulting in triplet scattering, as it results in a deeper scattering potential than singlet scattering [44]. The effects of the p-wave shape resonance are neglected for $n > 100$, because they only contribute within a limited spatial range [45].

The scattering potential (34) is introduced into the GPE, which models the effect of the single Rydberg atom on the BEC

$$i\hbar\frac{\partial}{\partial t}\psi(\boldsymbol{r},t) = \left[-\frac{\hbar^2}{2m}\nabla^2 + V_{\text{ext}}(\boldsymbol{r}) + g|\psi(\boldsymbol{r},t)|^2 + V_{Ryd}(\boldsymbol{r}-\boldsymbol{R})\right]\psi(\boldsymbol{r},t). \quad (35)$$

The Rydberg state's lifetime defines the time period during which the scattering potential has an effect. A ^{87}Rb atom excited to $n > 100$ in a BEC has an average lifetime on the order of 10 µs [5]. The interaction of the Rydberg electron with the BEC decays exponentially with a time constant, which is defined by the lifetime of the Rydberg state [6]. The Rydberg state's lifetime in a BEC is about two orders of magnitude shorter than its lifetime in a thermal cloud [47]. In a condensate l-changing collisions and chemical reactions, that shorten the lifetime, can occur [46, 47], due to the high density of the sample.

Although the lifetime of the Rydberg state is limited, it is nevertheless sufficient for the scattering potential to cause a phase imprint on the BEC. The resulting phase gradient in the medium generates a redistribution of the atoms in the BEC. The ground state atoms begin to rearrange themselves according to the attractive interaction. They experience a force towards regions of high Rydberg electron probability.

There are now two possible methods for continuing. The first is to simply wait, as the ground state atoms continue to redistribute themselves, enhancing the imprint of the Rydberg orbital onto the density distribution of the BEC. Strictly speaking with this technique we do not imprint the wave function, but in fact imprint the atomic orbital which is the absolute square of the wave function. After a period of time (on the order of hundreds of microseconds [6]) maximal contrast between high and low density is reached before the imprint begins to dissolve. An example of an image of a density imprint is depicted in figure 3 for the case of a 140D state.

The second option is to repeatedly pulse the excitation laser so that a new Rydberg atom is excited every time its predecessor has decayed. The achievable contrast is higher, but the resolution is reduced, as the Rydberg atom isn't excited in the exact same spot each time [5].

After the orbital has been imprinted onto the density of the BEC, it can be measured optically. Due to the density in the BEC simple absorption imaging cannot be used to image the density distribution, however it can be visualized via phase-contrast imaging [13].

The resulting image corresponds to an integration of the density inside the BEC along the imaging axis of the phase-contrast imaging.

An ideal image of the orbital is high in resolution and contrast. If the principle quantum number of the Rydberg atom is too small, the electron orbital, which scales with n^{*2}, is difficult to resolve. On the other hand a high principle quantum number results in a low contrast, because the effective scattering potential (34) scales with n^{*-6}. The effective scattering potential should be at least an order of magnitude deeper than the chemical potential in the BEC. Otherwise there is no sufficient phase imprint before the Rydberg atom decays [5]. The best images are expected for a principle quantum number between 100 and 160, because the orbital radius is large enough to be resolved and at the same time the potential is still sufficiently deep for providing a phase imprint with high contrast.

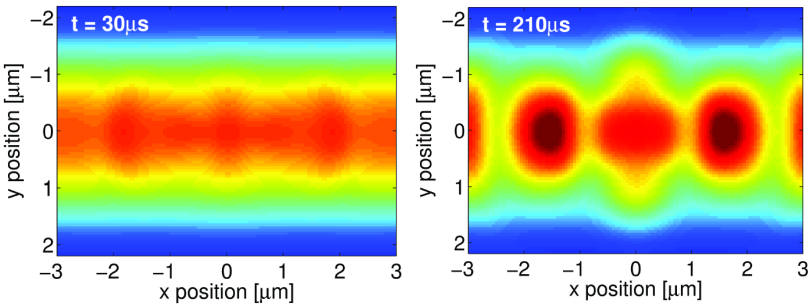

(a) image directly after decay (b) image after additional 180 µs

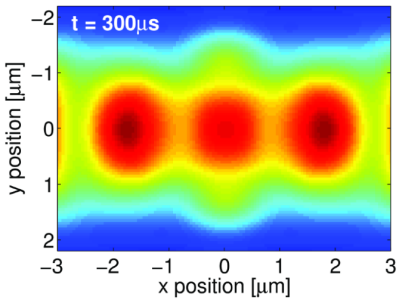

(c) image starts to dissolve

Figure 3: Time evolution of the imprint of a 140D Rydberg atom onto the density of the BEC. a) shows an image directly after the decay of the Rydberg atoms, which in this simulation had a lifetime of 30 µs , b) after about 180 µs the density distribution of the BEC shows maximum contrast before it starts to disolve as is shown c) [6].

In addition to that the density of the BEC also influence the quality of the image. High density in the BEC reduces the lifetime of the Rydberg state and thereby reduces the interaction time of the Rydberg electron with the BEC. In a dilute BEC there is more shot noise as a result of the smaller number of interacting atoms [6].

3.4 Experimental realisation

3.4.1 Single Rydberg excitation

In our experiment the Rydberg atoms are excited via 2-photon-excitation following the scheme depicted in figure 4. In some cases three-photon excitation can also be practiced. It is possible, in theory, to excite a Rydberg atom with a single photon, however that would require a light source at 297 nm [48], a wavelength which in practice is difficult to produce and problematic to work with due to lack of commercial optical elements for that specific wavelength. Another advantage of two-photon excitation is that it allows us to excite an atom from an S-state into an S- or D-state. That is not possible with a single-photon excitation scheme due to the dipole selection rules [48].

The Rydberg atom creates a blockade around itself, where no additional Rydberg excitation is possible (see chapter 3.2.4). If the blockade radius exceeds the width of the excitation beam, in this example the infrared laser with 1020 nm, then only a single Rydberg atom is excited. In the experiment the infrared beam has a waist of 2 µm [49]. For comparison, a ^{87}Rb atom excited to $n = 100$ has a blockade radius of 15 µm.

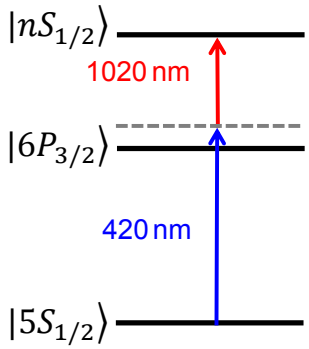

Figure 4: Example of a two-photon excitation scheme for exciting a ^{87}Rb atom to a Rydberg state.

3.4.2 Phase contrast imaging

Simple absorption imaging is not suitable for measuring the imprint of the Rydberg orbital, because the optical density of the BEC is too high to employ this technique. Instead phase contrast imaging [13] is applied.

The cloud is illuminated with a beam that has been so far detuned from resonance that dispersion is high, while absorption is low. Parts of the cloud with higher

density scatter the incoming light more strongly than dilute areas. The scattered light is redirected onto a phase plate and experiences a phase shift. By interfering with the unscattered light it creates an image of the density distribution of the ultracold cloud. Dense areas will appear bright on the camera due to constructive interference. In the schematic setup shown in figure 5, the image is additionally magnified before being projected onto a camera. An imaging system with high NA (numerical aperture) should be chosen in order achieve sufficiently high imaging resolution.

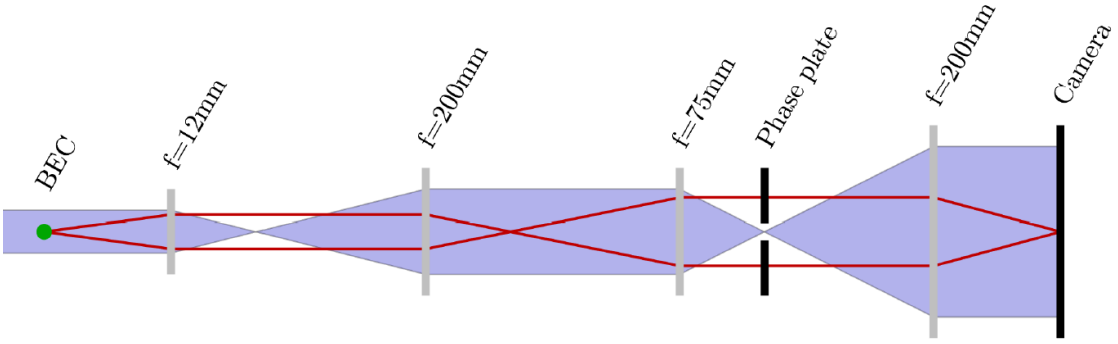

Figure 5: Schematic setup of the phase-contrast imaging system as it is currently implemented in the cold ^{8}7Rb atoms experiment. The blue area refers to the imaging beam. The red lines indicate the light that was scattered by the BEC [14]. The scattered light aquires a phase due to the phase plate and interfers with the non-scattered light on the camera.

3.4.3 Trapping potential of the BEC

The size of the trapped cloud should be similar in size to the Rydberg orbital, so that the background created by ground state atoms that haven't interacted with the Rydberg electron is as low as possible. However a cloud that is smaller than the Rydberg orbital can lead to a distorted image of the orbital [44].

Furthermore, the imaging contrast is expected to improve significantly for a flat quasi-2D trapping potential as compared to a cigar shaped potential formed by a typical magnetic quadrupole trap [6]. A simulated image of a single imprinted Rydberg orbital on a flat BEC is depicted in figure 6.

A pancake shaped cloud of atoms trapped in such a quasi-2d potential should be located inside the focal plane of the imaging system, perpendicular to the imaging axis. The creation of a trapping potential, capable of fulfilling the experimental demands of wave function imaging, is the goal of this master thesis.

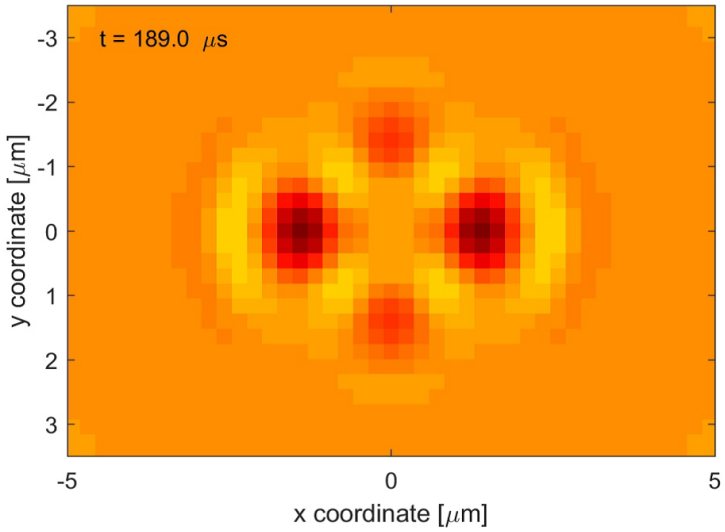

Figure 6: Simulated phase contrast image of a 140D orbital in a pancake shaped BEC with finite resolution of the imaging system after an evolution time of 189 µs. The simimulation is based on a the same code as in figure 3 [6] and has been adjusted for a pancake potential. The potential has a trapping frequency of 500 Hz along the direction of strong confinement and 8 Hz in perpendicular directions. A maximum contrast of 60 % is calculated for these parameters.

4 Dipole traps and lattices

This chapter focuses on the working principles and use of dipole traps and optical lattices. It is based mainly on R. Grimm and M. Weidemüller's article on optical dipole traps [50] and M. Lewenstein and A.Sanpera's review on ultracold lattice gases [51]. First an introduction to ultracold atoms in lattices and their application is given, followed by a theoretical description of the concept of trapping atoms in a dipole trap and an explanation of the heating mechanisms in such a trap. Lastly the behaviour of atoms in optical lattices is explored.

4.1 Ultracold atoms in lattices

Ultracold atoms trapped inside lattices, either as ensembles or as single atoms placed on individual lattice sites, are not only of interest for atomic physics but also for other fields of research. The reason for this is the sheer range of possible systems which can be represented and simulated by ultracold lattice gases.

The trapping potentials of optical lattices and dipole traps in general are extremely versatile. Three-dimensional lattices can be used to simulate cubic or hexagonal crystal structures without any defects [52, 53], thereby serving as a platform for simulating solid-state phonemena. Solid-state physics uses the Hubbard model as a simplified representation of a solid with strongly interacting electrons and it can be well simulated with cold atoms in a lattice [54, 55]. These insights could be important for investigating effects like high-temperature-superconductivity [56, 57], superfluid to Mott-insulator transition [58] or the metal-insulator transition [59].

Optical lattices can create perfect regular structures with high symmetry. However it is also possible to create purposefully disordered systems [60], for example by using speckle radiation or overlapping lattices with different spacings [61]. Controlled disorder is relevant for condensed matter physics, as it is essential for the study of delocalisation [62], but also for investigating spin-glasses [63, 64], spin-liquids [65] and the disordered Ising model [66], which is the basis for the understanding of quantum magnetism.

In addition to that, dipole traps and lattices also allow measurements with a reduced number of dimensions: two-dimensional systems [58, 66] and even one-dimensional systems [67] can be realised.

Lattices are also key components in experiments of quantum information, quantum computation and topology [68, 69, 70].

The application of lattices is not limited to the field of physics but extends to chemistry as well. The controlled formation of molecules in an optical lattice has been achieved for example by the group of Jun Ye et al. [71].

In summary, ultracold atomic gases in optical lattices are highly versatile instruments and offer insights into many fields of physics.[51]

4.2 Dipole force

Intersecting two or more beams creates different kinds of optical lattices, such as cubic or hexagonal lattices, depending on the orientation of the beams. In all the examples mentioned above the optical lattice acts as a dipole trap for the atoms. The working principle of dipole traps in general is explained in this chapter.

Within a monochromatic laser beam atoms experience a force along the intensity gradient called dipole force.

In order to understand the origin of this force, one can consider the electron inside the atom to be an oscillator driven by an external laser field. This classical approach is called the Lorentz model [72]. The electric field component $\vec{E}$ of the light induces a dipole moment $\vec{p}$ within the atom. The field $\vec{E}$ oscillates at the laser frequency ω and can be written as

$$\vec{E}(\vec{r},t) = E_0(\vec{r}) \cdot \exp(-i\omega t) \cdot \vec{e} + c.c.. \tag{36}$$

$E_0(\vec{r})$ is the amplitude of the electric field and it is pointing in the direction of $\vec{e}$, the unit polarisation vector. The induced dipole moment $\vec{p}$ of the atom can be defined likewise as

$$\vec{p}(\vec{r},t) = p_0(\vec{r}) \cdot \exp(-i\omega t) \cdot \vec{e} + c.c. = \alpha(\omega) \cdot \vec{E}(\vec{r},t). \tag{37}$$

$\alpha(\omega)$ is the complex polarisability of the atom. With knowledge of the dipole moment and the driving field $\vec{E}$, an interaction potential can be formulated using the time average of the two

$$U_{dipole} = -\frac{1}{2}\langle \vec{p}\vec{E} \rangle. \tag{38}$$

Using the fact that the field intensity I is defined as

$$I = 2\epsilon_0 c |E_0|^2, \tag{39}$$

the potential in equation (38) can be rewritten as

$$U_{dipole} = -\frac{1}{2\epsilon_0 c}\mathrm{Re}(\alpha) \cdot I(\vec{r}). \tag{40}$$

The negative gradient of the interaction potential is the dipole force

$$\vec{F}_{dipole}(\vec{r}) = -\nabla U_{dipole} = \frac{1}{2\epsilon_0 c}\mathrm{Re}(\alpha) \cdot \nabla I(\vec{r}). \tag{41}$$

The scattering rate of the photons is calculated with the imaginary part of the polarisability

$$\Gamma_{sc} = \frac{1}{\hbar\epsilon_0 c}\mathrm{Im}(\alpha) \cdot I(\vec{r}) \tag{42}$$

and can also be understood as the ratio between the absorbed power P_{abs} and the photon energy

$$\Gamma_{sc} = \frac{P_{\mathrm{abs}}}{\hbar\omega}. \tag{43}$$

The Lorentz-model defines Γ as the on-resonance damping of the electron's motion. A semi-classical approach to the problem is also possible. In this case the atom is viewed as a quantum object and is reduced to a two-level system with a ground state and an excited state, while the light is described as a classical radiation field. The damping rate Γ is then determined by the dipole matrix element $\mu = e \cdot \vec{r}$ between the ground state $|g\rangle$ and the excited state $|e\rangle$

$$\Gamma = \frac{\omega_0^3}{3\pi\epsilon_0\hbar c^3}|\langle e|\mu|g\rangle|^2 \tag{44}$$

and corresponds to the spontaneous decay rate from the excited level. Dipole traps in general operate at frequencies far detuned from the atomic resonance. This significantly reduces photon scattering, subsequent heating and avoids saturation. The dipole potential and the scattering rate can then be written as

$$U_{dipole}(\vec{r}) = -\frac{3\pi c^2}{2\omega_0^3}\left(\frac{\Gamma}{\omega_0-\omega}+\frac{\Gamma}{\omega_0+\omega}\right)I(\vec{r}), \tag{45}$$

$$\Gamma_{sc}(\vec{r}) = \frac{3\pi c^2}{2\hbar\omega_0^3}\left(\frac{\omega}{\omega_0}\right)^3\left(\frac{\Gamma}{\omega_0-\omega}+\frac{\Gamma}{\omega_0+\omega}\right)^2 I(\vec{r}). \tag{46}$$

If the detuning $\Delta = \omega - \omega_0$ is large enough to neglect saturation, but the driving frequency is still chosen at $|\Delta| \ll \omega_0$, then this would allow us to use the so-called rotating wave approximation. The dipole potential can thus be simplified to

$$U_{dipole}(\vec{r}) = \frac{3\pi c^2}{2\omega_0^3}\frac{\Gamma}{\Delta}I(\vec{r}) \propto \frac{\Gamma}{\Delta}I(\vec{r}) \tag{47}$$

with a scattering rate of

$$\Gamma_{sc}(\vec{r}) = \frac{3\pi c^2}{2\hbar\omega_0^3}\left(\frac{\Gamma}{\Delta}\right)^2 I(\vec{r}) \propto \left(\frac{\Gamma}{\Delta}\right)^2 I(\vec{r}) \tag{48}$$

Equations 47 and 48 show why dipole traps for cold atoms often use light with very high intensity and large detuning at the same time. The potential becomes deeper for higher intensity. In addition the radiation force due to photon scattering is reduced to a negligible value compared to the dipole force by choosing light with a frequency which is far detuned from the atoms' resonance frequency ($\Gamma \ll |\Delta|$), which reduces the loss due to heating. In summary the dipole force depends on the detuning, the damping rate and the intensity gradient (∇I)

$$\vec{F}_{\text{Dipole}} \propto -\frac{\Gamma}{\Delta}\nabla I(\vec{r}). \tag{49}$$

The sign and therefore the direction of the dipole force now depends on the sign of the detuning. Blue detuned light ($\Delta > 0$) causes the atoms to move towards lower intensity, while red detuning ($\Delta < 0$) results in a force towards the intensity maximum. The focus of a red detuned Gaussian beam is the simplest example of such a trap and is referred to as an optical tweezer [73].

While these equations describe a simplified atom as a two-level-system, real atoms have multitudes of levels. However the behaviour described in equation 49 remains the same, even if the atomic sub-structure is taken into account.

Alkali atoms for example have a very characteristic splitting of the D-line, the transition from $n^2S_{1/2}$ to $n^2P_{1/2}$ and $n^2P_{3/2}$. If the detuning largely exceeds this splitting, then the hyperfine-structure can be completely neglected. For linearly polarised light ($\mathcal{P} = 0$), the dipole potential remains exactly as it has been defined in equation 47. The detuning Δ is then defined relative to the center of the D-line dublett. For circular polarisation ($\mathcal{P} = \pm 1$) of the incoming laser light an additional correction term is added

$$U_{\text{dipole}}(\vec{r}) = \frac{3\pi c^2}{2\omega_0^3}\frac{\Gamma}{\Delta}\left(1 + \frac{1}{3}\mathcal{P}g_F m_F \frac{\Delta'_{\text{FS}}}{\Delta}\right) I(\vec{r}), \tag{50}$$

which also includes the Landé factor g_F and the magnetic sub-state m_F. Δ'_{FS} is the fine-structure splitting and is typically significantly smaller than the detuning. Therefore the last term is often neglected, again reducing the alkali atom to a simple two-level-system with only one relevant transition $s \to p$.

4.3 Heating mechanisms in dipole traps

The dipole force is a conservative force. In consequence it cannot be used for cooling, only for trapping. As optical dipole traps use far detuned light, optical excitation is very low. Typically such traps have a depth in a range lower than 1 mK, which is why atoms have to be cooled down prior to being loaded into the trap. In consequence if the atoms gain too much kinetic energy through any kind of heating process, the atoms will eventually leave the trap [50].

The origins of heating in dipole traps is explored in this section.

One important source of heating comes from spontaneous scattering of photons. The scattering process consists of absorption of a photon and spontaneous emission in a random direction. This causes fluctuations of the radiation force and thus heating. In the case of far detuned light, the scattering can be considered to be elastic [50].The heating power is given by

$$P_{\text{heat}} = 2E_R\bar{\Gamma}_{\text{sc}} = k_{\text{B}}T_R\bar{\Gamma}_{sc}. \tag{51}$$

E_R and T_R refer to the recoil energy and the corresponding recoil temperature, $\bar{\Gamma}_{sc}$ is the average photon scattering rate. For the far-detuned case the scattering rate Γ_{sc} decreases drastically, which makes heating due to photon scattering negligible, especially compared to heating due to technical limitations.

Heating can result from fluctuations in the potential caused by instability in intensity and spacial instability (position of the trap). This kind of heating strongly depends on the technical specifications of the laser used. For typical trap frequencies of dipole traps, the intensity noise and beam-pointing noise of the laser in the kHz range are relevent. To name an example, ^{87}Rb atoms, that are trapped a focussed Gaussian beam with a power of 1 W and a beam waist of 50 µm, have a trapping frequency of 2.4 kHz.

Let's first take a look at heating through intensity fluctuations. We assume a harmonic potential (in close approximation). The motion of the trapped atom with mass m can be described with a mean square trap frequency $\omega_x^2 = k_x/m$ and a spring constant k_x along one axis. In the case of a far-detuned Gaussian beam with a $1/e$-intensity radius a the spring constant can be written as $k = 2U_0/a^2$, wherein U_0 is the maximal potential depth. This means that the spring constant is proportional to the laser intensity. The Hamiltonian for a trapped atom under these circumstances can be written as

$$H = \frac{p^2}{2m} + \frac{1}{2}m\omega_x^2(1 + \epsilon(t))x^2 \tag{52}$$

with the fractional fluctuation of the laser intensity being represented by $\epsilon(t)$. It is defined by

$$\epsilon(t) = \frac{I(t) - I_0}{I_0} \tag{53}$$

In order to derive the heating rate the Hamiltonian (52) can be solved via first-order time-dependent perturbation theory. The second harmonic of the trapping frequency leads to dominant parametric heating, because the Hamiltonian and the perturbative term share the same spacial symmetry. The resulting time dependence of the energy is exponential as shown in [74]

$$\langle \dot{E}_x \rangle = \Gamma_x \langle E_x \rangle \tag{54}$$

with an exponential rate of

$$\Gamma_x = \pi^2 \nu_x^2 S_k(2\nu_x). \tag{55}$$

$\nu_x = \omega_x/2\pi$ is the trapping frequency and S_k is the one-side power spectrum of the fractional fluctuation of the spring constant k_x. It is defined so that

$$\int_0^\infty d\nu S_k(\nu) = \langle \epsilon^2(t) \rangle, \tag{56}$$

which is the mean square fractional fluctuation in the spring constant [74].

The other source of parametric heating is instability in beam-pointing. It is characterised by the following Hamiltonian

$$H = \frac{p^2}{2m} + \frac{1}{2}m\omega_x^2(x + \epsilon_x(t))^2 \tag{57}$$

This time $\epsilon_x(t)$ is the fractional fluctuation of the position of the trap, more precisely, of the trap center. Similarly to the heating through intensity fluctuations, the heating rate can be again calculated via perturbation theory. This time however the result is a linear behavior [74]

$$\langle \dot{E}_x \rangle = \frac{\pi}{2} m\omega_x^4 S_x(\omega_x). \tag{58}$$

In contrast to equation (55), here the heating is independent of the trap energy $\langle E \rangle$. The power spectrum is defined similar to equation (56)

$$\int_0^{\inf} d\nu S_x(\nu) = \langle \epsilon_x^2(t) \rangle = \epsilon_x^2 \tag{59}$$

wherein ϵ_x^2 is the mean square variation of the trap position [74].

Atoms start leaving the trap when their mean energy $\langle E(t) \rangle$ is close to or above the potential depth U_0.

According to [75] the rate with which the atoms are lost depends not only on the parametric heating rate, but also on the initial conditions. If the mean energy of the atoms loaded into the trap is well below the potential depth of U_0, the population inside the trap decays at a smaller rate, than if the trap is loaded at a temperature similar to the trap depth. While this makes a dipole trap with higher intensity favourable, a deep potential well in combination with tight confinement also increases the effect of the fluctuations.

4.4 Tunneling between lattice sites

The heating mechanisms described in the previous section are not the only reason atoms can leave a potential well. Within an optical lattice atoms can tunnel from one lattice site into a neighbouring site. The tunneling rate depends on the on the potential depth and the lattice spacing. Tunneling can be surpressed by the potential difference between neighbouring latice sites.

4.4.1 Recoil energy

Imagine for example an optical lattice potential created by two counter -propagating narrow-band laser beams, each with Gaussian beam profiles and a beam waist of w_0. The resulting dipole potential in cylinder coordinates is

$$U(r, z) = -U_0 \exp\left(\frac{-2r^2}{w_0^2}\right) \sin^2(\frac{\pi z}{s}). \tag{60}$$

In this example the beams are propagating along the z-axis and $s = \pi/k$ is the lattice spacing and is defined by the wavelength of the counter-propagating beams, in this case $s = \lambda/2$. The spacing of an accordion lattice is defined by the wavelength and the angle of two intersecting beams (see chapter 5.2 for details). U_0 denotes the potential depth and is often stated in terms of temperature $U_0 = k_B T$. If U_0 is sufficiently deep, the individual potential wells in the lattice can be approximated as a harmonic potential and a trapping frequency ω_{tr} in direction of propagation can be defined as

$$\omega_{tr} = \sqrt{\frac{2U_0}{m}} k \tag{61}$$

with m being the mass of a trapped particle [76]. The recoil energy E_R in such a potential is

$$E_R = \frac{\hbar^2 k^2}{2m} = k_B T_R. \tag{62}$$

T_R is the corresponding recoil temperature. The potential depth is often given in multiples of the recoil energy [77].

4.4.2 Bloch states

The motion of a quantum particle in a one-dimensional potential in general is defined by a Hamiltonian

$$\hat{H} = \frac{\hat{p}}{2m} + U(x). \tag{63}$$

If the potential $U(x)$ is spatially periodic, then the eigenstates that solve the stationary Schrödinger equation

$$\hat{H}\,|\phi_{n,q}(x)\rangle = E_n(q)\,|\phi_{n,q}(x)\rangle \tag{64}$$

are the Bloch functions $|\phi_{n,q}(x)\rangle$, which have the same spatial periodicity as the potential $U(x)$ [77]. Here n denotes the energy band index, which will be explained below and q is the quasimomentum. The Bloch functions take the form

$$\phi_{n,q}(x) = \exp(iqx) \cdot u_{n,q}(x). \tag{65}$$

The function $u_{n,q}(x) = u_{n,q}(x+s)$ has the same periodicity s of the potential $U(x) = U(x+s)$. Due to the periodicity both the potential and the Bloch functions can be written in a Fourier series

$$U(x) = \sum_l U_l \exp(ilGx), \tag{66}$$

$$\phi_{n,q}(x) = \sum_l c_l^n \exp(iqx + ilGx). \tag{67}$$

The reciprocal lattice vector is defined as $G = 2\pi/s$ [77]. Using this ansatz in the stationary Schrödinger equation and limiting l to $|l| \leq \mathcal{N}$, the result is a $2(2\mathcal{N}+1)$-dimensional linear system of equations of the shape

$$\begin{aligned}\left(\frac{\hbar^2}{2m}(q - lG)^2 + U_0\right) \cdot c_{q-lG} + U_G \cdot c_{q-(l+1)G} \\ + U_{-G} \cdot c_{q-(l-1)G} = c_{q-lG} \cdot E\end{aligned} \tag{68}$$

with $l = -\mathcal{N}, -\mathcal{N}+1, ..., \mathcal{N}-1, \mathcal{N}$ [77]. Equation (68) produces $2\mathcal{N}+1$ different eigenenergies E_n with $n = 0, 1, 2, ..., 2\mathcal{N}$ for given quasimomentum q. The quasimomentum q can be restricted to $-\hbar k \leq q \leq \hbar k$, which is the first Brillouin zone. In the case of a sinusoidal potential with lattice spacing s the wave vector is $k = \pi/s$. In the case of deep lattice potentials, it is often sufficient to only consider the lowest bands. For example in the case of $U_0 \leq 20E_R$ is it enough to take $|l| \leq 5$ into account [76], only the lowest bands are of interest.

Figure 7 shows the dispersion relations $E_n(q)$ for different potential depths in the first Brillouin zone. The eigenenergy spectrum is separated into energy bands E_n by the lattice potential. There are gaps of forbidden energy values in between the energy bands and the energy gaps become larger for deep lattices while the bands become narrower. The lowest band's dependence on q also decreases with increasing potential depth.

The Bloch states are delocalised over the entire lattice [78].

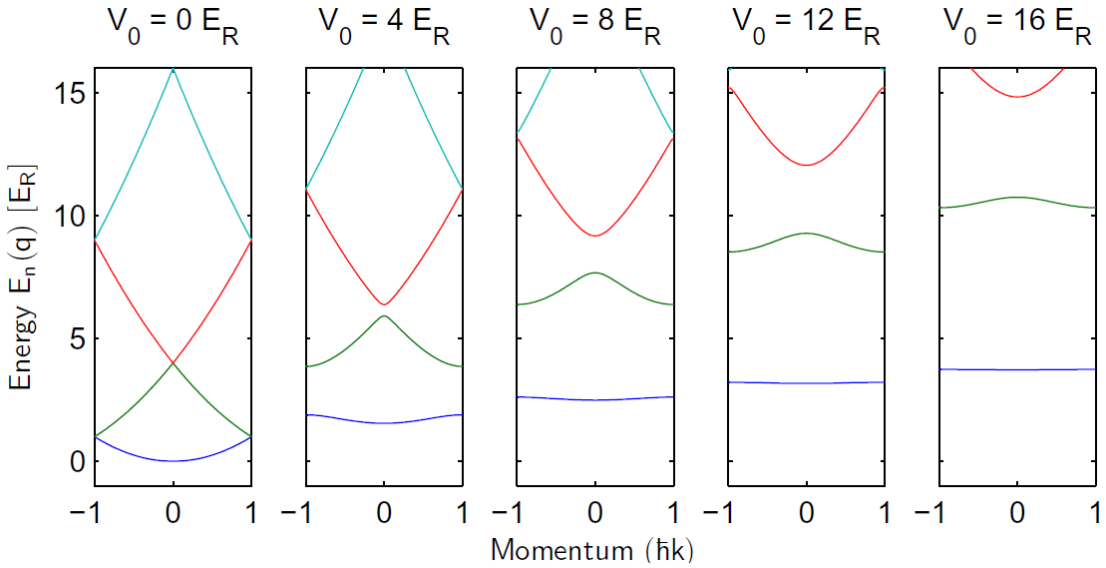

Figure 7: Energy bands $E_n(q)$ for different potential depths within the first brillioun zone. The potential depth of $U_0 = 0E_R$ corresponds to a free particle. [76]

4.4.3 Wannier states

In deep lattices ($U_0 \gg E_R$) only the lowest band is taken into account and the wave functions can become localised within certain potential wells. In that case the Bloch states are no longer a convenient basis for calculation. Instead the Wannier states are introduced, which comprise of a superposition of all Bloch states in one energyband [77]. The Wannier states provide a single-particle basis that is well suited for the case of deep, discrete lattice sites, where the particle is localised in a specific potential well. They are connected to the Bloch states by a Fourier transformation

$$w_n(R,x) = \frac{1}{s}\int \mathrm{d}q\; exp(-iqR)\phi_{n,q}(x) \tag{69}$$

and is centered around the lattice site R [77], with $R = u \cdot s$, $u \in \mathbb{N}$. They fulfill the orthonormality relation for different sites R and energy bands n

$$\int \mathrm{d}\vec{r}\; w_n^*(r-R_u)w_{n'}(r-R_v) = \delta_{n,n'}\delta_{u,v} \tag{70}$$

4.4.4 Tunneling matrix element J

A particle that tunnels from one potential well into a neighbouring well requires a certain amount of kinetic energy. This energy can be described by the parameter $J > 0$, also defined as the tunneling matrix element or hopping matrix element in context of the tight binding model [78]. In general J is detemined by the energies $E_n(q)$ of the Bloch energy bands. For particles trapped in a deep lattice ($U_0 \gg E_R$), it is sufficient to only take into account the lowest band and next nearest neighbour tunneling.

The tunneling matrix element can be interpreted as the overlapp between two localised wannier states [77]

$$J = -\int \mathrm{d}\vec{r} \left(\frac{\hbar^2}{2m} \nabla w_u \cdot \nabla w_{u+1} + w_u U_{\mathrm{ext}} w_{u+1} \right). \tag{71}$$

In the case of deep lattices the tunneling matrix element J can be approximated using

$$\frac{E_n(q)}{E_R} = \sqrt{\frac{U_0}{E_R}} - 2J\cos(qs) \tag{72}$$

and

$$J = \frac{4}{\sqrt{\pi}} E_R \left(\frac{U_0}{E_R} \right)^{3/4} \exp\left[-2 \left(\frac{U_0}{E_R} \right)^{1/2} \right], \tag{73}$$

which is obtained by analytically calculating the eigenenergies of the lowest band in the limit of deep periodic potentials, also called the tight binding limit [79]. According to equation (72) the energy gain J corresponds to four times the with of the lowest energy band. For finite potential depths equation (73) is only an approximation for J. For a potential depth of $U_0 > 15E_R$ for example it can estimate J with an accuracy of about 10 % [78]. The tunneling matrix element can be used to determine a characteristic time for tunneling as $T_{tun} = 2\pi\hbar/J$, which means, if J is smaller than the Planck constant, the characteristic time for tunneling is more than one second. In the context of cold atoms experiments one second is often considered an extremely long time compared to other time scales, like for instance lifetimes of Rydberg atoms on the scale of a few µs.

Figure 8 shows a calculation of the tunneling rate J/h as a function of the potential depth using equation (73). The calculations were performed for five different lattice spacings, which are realised by a counter-propagating beam of 1064 nm light and by the accordion lattice that is characterised in this thesis. For the potential range depicted in figure 8 the approximation of a deep lattice potential is valid. For the example of the accordion lattice, tunneling can be completely neglected. For the case of the counter-propagating beam, the spacing is an order of magnitude smaller than the smallest spacing in the accordion. For such lattice with such a small spacing, tunneling may be relevant, depending on the timescale of the experiment. At a potential depth of 500 nK, the tunneling rate would still be below 100 Hz.

In conclusion, tunneling decreases for deep potentials with wide lattice spacing s. In addition, tunneling is forbidden due to energy conservation, if neighbouring lattice sites have a potential difference of $\Delta U_0 > J$ [76].

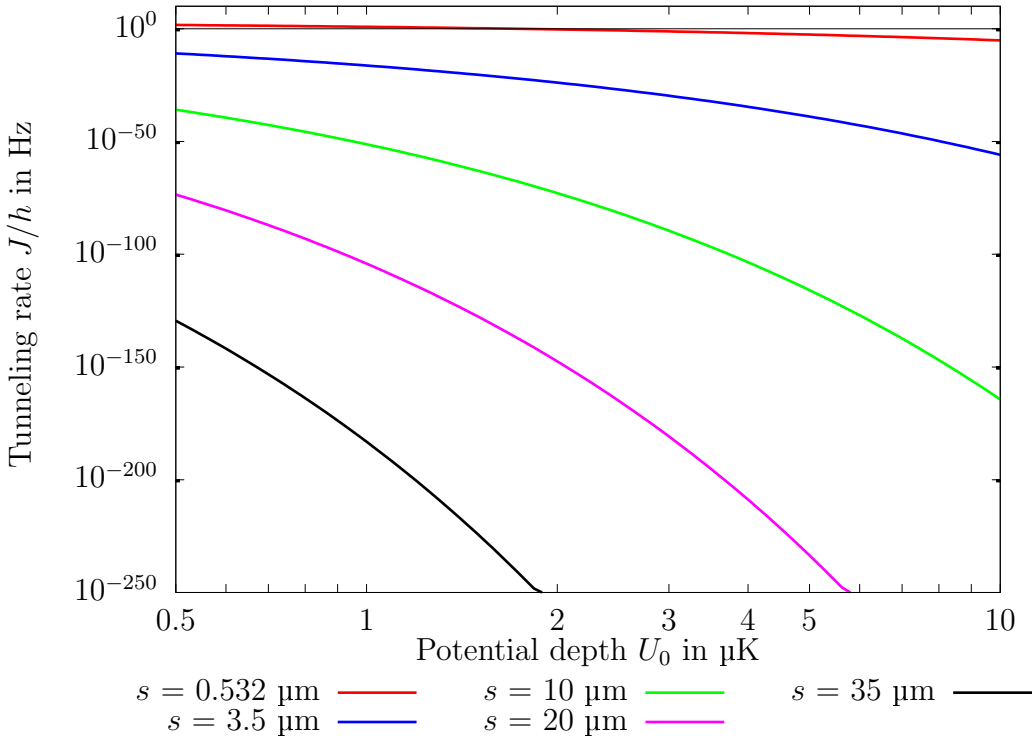

Figure 8: A calculation of the tunneling rate J/h as a function of the potential depth using equation (73) for deep lattice potentials. J is calculated for trapped ^{87}Rb atom in a counter-propagating beam of 1064 nm light (s=0.532 µm), as well as for different lattice spacings realised by the accordion lattice, described in this thesis. The tunneling rate increases with smaller lattice spacings and decreasing potential depth. In this example tunneling is only significant for the counter-propagating trap. It can be completely neglected in the case for the accordion lattice.

5 Experimental setup

This chapter focusses on the experimental realisation of the accordion lattice. First the technical requirements are specified, followed by a schematic, a description of the setup and an explanation of the working principle of the accordion lattice in section 5.2. This chapter also includes a characterisation of the camera, as it is the main instrument for measurement in this thesis.

5.1 Experimental requirements

Within the scope of this thesis an accordion lattice for trapping ultracold ^{87}Rb atom is develloped. In order to be able to use the trapped atoms in an experiment, that enables the imaging of the electronic orbital of a Rydberg atom, several experimental requirements have to be fulfilled, which will be explained in the following.

Laser frequency and stability

The laser frequency for the dipole trap has to be far detuned from the atomic resonance, otherwise the atoms will leave the trap due to the parametric heating already described in chapter 4.3. A trapping time on the scale of at least tens of milliseconds is desired. This means the laser intensity and beam pointing has to remain as stable as possible, on short timescales in order to avoid heating, and on long timescales to be able to obtain reproducible results.

Furthermore the wavelength has to be $\lambda > 1010\,\text{nm}$, otherwise it would result in ionisation of the Rydbergatom in combination with the 420 nm light from the two-photon excitation. As a lot of the measurements performed inside the science chamber rely on ionisation as a method of detecting Rydberg excitation, any additional ionisation by trap light has to be avoided.

Spatial requirements

The ultracold atoms reside inside a vacuum inside a glass chamber. Optical access is limited by the size of the windows. The window has a height of 12 mm and is 13 mm away from the cloud of atoms in the center of the vacuum. This means, that two beams can intersect with an angle less than 24° without being clipped by the window.

Since the accordion lattice will be integrated into a versatile and therefore complex cold atom experiment, the size of the setup is desired to be as compact as possible. Especially the coil holders around the glass cell obstruct any addtional optical setup. It is therefore not possible to position elements of the setup closer than about 150 mm close to the atom cloud. This distance is set by the distance between the glass cell and the surrounding coil holders. As space on the entire optical table is very limited, the setup has to be as compact as possible and the distance between the setup and the actual dipole trap has to be at least 150 mm.

Confinement and orientation

As has already been stated in section 3.4.3, a flat, pancake shaped trapping potential perpendicular to the imaging axis provides the best contrast for wavefunction imaging. In consequence, for best results the potential has to provide very tight confinement on the range of a few µm (roughly the size of the Rydberg orbital) along the axis of the imaging beam and weak confinement in perpendicular directions. The beam used for imaging enters the science chamber from the top and is reflected by a mirror below the chamber onto a camera through an imaging system for phase contrast imaging. Therefore the dipole trap has to be aligned horizontally.

The trapped atoms have to remain within the focal depth of the imaging system which is only a few µm. If the pancake shaped cloud of atoms drifts outside this plane the resolution of the obtained images is drastically decreased.

In addition, it is required, that the trap can be loaded by overlapping with the magnetic quadrupol trap, that holds the atoms. Therefore a potential well has to be of similar size as the extent of the magnetic trap. The latter provides a cigar shaped confinement which is between 5 µm and 10 µm wide and ten times as long.

In order to fulfill these requirements a dipole trap called an accordion lattice is chosen. The design and its function is explained on the following pages.

5.2 Schematic setup

This section covers the working principle of the accordion lattice, including a schematic of the setup, which is displayed in figure 9 .

The working principle of the accordion lattice is the intersection of two identical laser beams at a variable angle, resulting in an interference pattern at the intersection. First a single 1064 nm beam passes a $\lambda/2$-waveplate and is reflected on the mirror M1. The mirror is mounted at a 45° angle. The beam is reflected into a polarising beam splitter cube (PBS1), which splits the light into two linear polarised components. The s-polarised component is reflected by the cube, the p-polarised component passes through a second beam splitter cube (PBS2) without deflection. It is reflected back of a mirror M2. Between the second cube (PBS2) and the mirror (M2), there is a $\lambda/4$-waveplate. Therefore the reflected beam passes the $\lambda/4$-waveplate twice and is consequently s-polarised. The beam reenters the beamsplitter (PBS2) and is reflected.

The result is two parallel laser beams with identical polarisation. The two beams are crossed by a lens (L1) and create an interference pattern consisting of many layers at their intersection. To achieve maximal contrast in the interference pattern, both intersecting beams need to have the same intensity. The intensity of the beams in relation to each other can be tuned with the $\lambda/2$-waveplate.

The spacing of the pattern depends on the angle with which the beams intersect. By changing the angle the spacing can be varied.

The mirror M1, which reflects the single beam into the cubes, is mounted on top of a motorized stage. It can be precisely displaced, thereby changing the distance

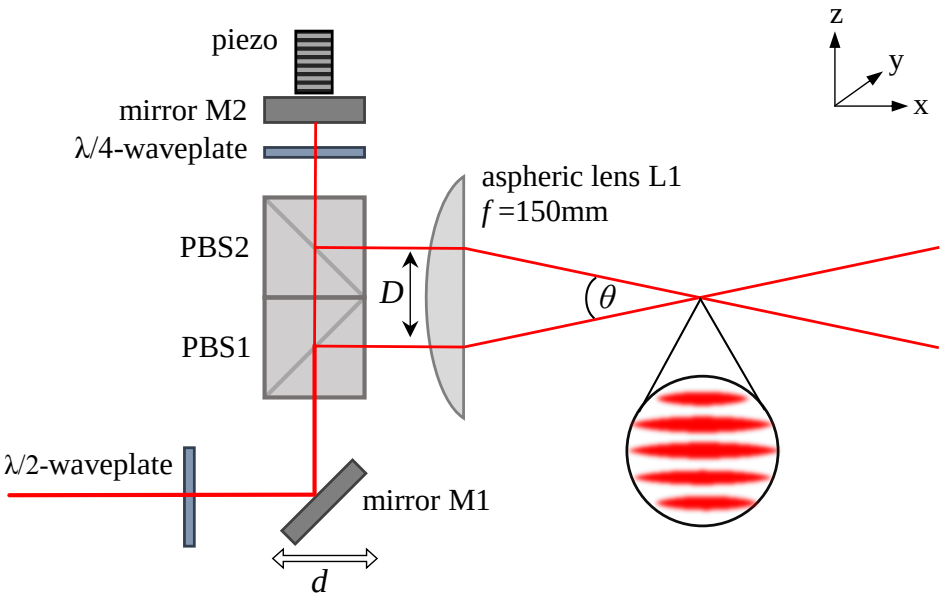

Figure 9: Schematic setup of the accordion lattice. The 1064 nm laser light is reflected on mirror M1, which is mounted on a translation stage. The stage can be displaced by d, which also changes the distance D between the two parallel beams, that are crossed by the lens L1. The interference pattern at the point of intersection is indicated inside the circle. The lattice planes are stacked along the z-axis.

between the two parallel beams and the resulting angle of intersection. Sperical aberations in the lens (L1) can cause the position of the interference pattern to change, when the angle of intersection is varied. This effect is minimised by using an aspherical lens.

When using the accordion lattice as a dipole trap, the atoms are loaded into a single plane of the interference pattern at large spacing. This is done by overlapping the lattice with a magnetic trap that hold the atoms. By then moving the mirror on the stage, the spacing is reduced and confinement along the z-axis is increased to the desired value. The loading of the trap at large spacing avoids the population of multiple layers within the lattice.

For the pancake potentials to be perpendicular to the imaging beam of the phase imaging system, the polarising beam cubes (PBS) have to be mounted vertically, stacked on top of one another. The accordion lattice only provides strong confinement along the z-axis. The trapped atoms are still able to escape the trap in the direction of beam propagation. Therefore additional confinement in the xy-plane is needed. For that a second beam can be implemented, which propagates along the z-axis and is perpendicular to trapping potential provided by the accordion lattice. This additional beam along the z-axis can be for example a 1064 nm gaussian beam. This thesis will however place its main focus on the confinement created by the accordion lattice.

In order to be able to use the atoms trapped in the accordion lattice for wave function imaging, the layer of atoms has to remain spatially stable within the focal plane of the imaging system used for the phase contrast imaging, otherwise the resolution of the images is descreased. The position of the layers within the interference pattern depends on the relative phase between the two intersecting beams. The phase is defined by the difference in the optical path length between the two intersecting beams. With perfect alignment this difference is exactly twice the distance between the first cube (PBS1) and the second mirror (M2). However, this distance can vary due to temperature fluctuations and the subsequent thermal expansion of the setup.

Thus, a mechanism to actively compensate the phase has to be implemented into the system. This can be achieved by adding a piezo stack to the back of the mirror M1. By applying a voltage to the piezo stack, phase drifts can be compensated. The phase information needed to apply the correct voltage is obtained by imaging the lattice onto a camera and extracting the phase from the data. A PID-controller (proportional-integral-derivative controller) can be used to stabilise the phase at a desired value. Details concerning the phase stabilisation can be found in chapter 7.

In order to achieve a deep dipole potential with little parametric heating, a laser with a wavelength of 1064 nm was chosen. It provides large, red detuning relative to the 5S to 5P transition in Rubidium while at the same time avoiding heating and ionisation. Lasers as well as optical components designed for this wavelength are commercially available. The laser used for this setup is a NKT Koheras Boostik, which is designed to have low intensity and phase noise.

The aspheric lens L1 (see figure 9) has a focal length of 150 mm and a diameter of 750 mm. All other optical elements are one inch in diameter. This means that two intersecting beam cross at an angle of less than 19° and the distance between the setup and the atoms is 150 mm to fulfill the spatial requirements of the apparatus. The Gaussian optics waist in front of the setup is $w_0 = 520$ µm, therefore the width in the focal point of the lens is $w' = 97$ µm.

Mirror M1 in the setup (see figure 9) is mounted atop a motorised stage, so that it can be displaced fast and smoothly. A MTS25/M-Z8 motorised translation stage from Thorlabs was chosen. It has a translation range of 25 mm, which is needed to displace the beam along the whole width of the polarising cubes. In addition it is smaller in size than comparable models, which means it would consume less space on the optical table. Position and speed can be set via a controller, which can be externally triggered to perform a predefined action. The trigger signal is a TTL signal. In consequence the motion of the stage can be triggered by a voltage signal from a Raspberry Pi for example.

The spacing in an interference pattern from two intersection beams is given as follows:

$$s = \frac{\lambda}{2\sin(\theta/2)}. \tag{74}$$

wherein λ is the wavelength of the laser light and θ is the angle between the two beams. The intersection angle can be calculated from the distance of the parallel beams and the geometry of setup.

$$\frac{\theta}{2} = \arctan\left(\frac{D}{2f}\right). \tag{75}$$

D is the distance between the parallel beams and f is the focal length of the aspherical lens. D can also be written in terms of the mirror displacement d on the stage with d_0 as the starting position:

$$D = 2(d + d_0). \tag{76}$$

The spacing can then be written as a function of wavelength, focal length and mirror displacement.

$$s = \frac{\lambda}{2}\sqrt{1 + \left(\frac{f}{d + d_0}\right)^2} \tag{77}$$

The values for the setup described in this thesis are $\lambda = 1064\,\mathrm{nm}$, $f = 150$ mm and $4\ \mathrm{mm} \leq D \leq 46$ mm, taking into account, that any clipping of the beams at the edges of the cubes has to be avoided. This yields a spacing range of $40\ \mu\mathrm{m} \geq s \geq 3.5\ \mu\mathrm{m}$.

In our case $\left(\frac{f}{d+d_0}\right)^2 \gg 1$, which allows the following approximation to be made with a deviation from equation (77) of about 1 %

$$s \approx \frac{\lambda}{2} \cdot \frac{f}{d + d_0} \tag{78}$$

As the wavelength as well as the focal length are fixed values in this setup, one has absolute control over the spacing via the mirror on the stage. The spacing is limited by the size of the optical components and the beam width, clipping of the beam has to be avoided. By applying a voltage to the piezo, which is depicted in figure 9, the phase of the lattice fringes within the Gaussian envelope can be adjusted. That means we have absolute control over spacing and phase within the lattice by controlling the position of the mirror on the stage and voltage on the piezo stack.

5.3 Characterisation of the Pi Camera

For most measurements as well as for the feedback loop a Raspberry Pi NoIR camera was used in combination with a Raspberry Pi 3. This particular camera has no inbuilt infrared filter and is therefore suited to measuring light at a wavelength of 1064 nm, which is in the near-infrared region. The camera uses a Sony IMX219PQ CMOS-chip. Like most standard camera-chips, it mimics the perception of the human eye, which means that the response does not behave linearly with increasing intensity. The human eye perceives increasing light intensity with a near logarithmic behaviour. As the camera is the main measurement instrument used in this thesis, characterisation measurements of the chip are appropriate.

The Raspberry Pi Camera has several settings which can be varied, such as resolution, shutter speed or the ISO (International Organization of Standardization), which is a standardised value for light sensitivity. Furthermore the chip has pixels that are sensitive to three colours: red, green and blue. The data of each color can be evaluated separately.

For all characterisation measurements in this chapter the camera is placed in the focus of the setup where the two beams cross (see figure 9).

5.3.1 Comparison of the colours

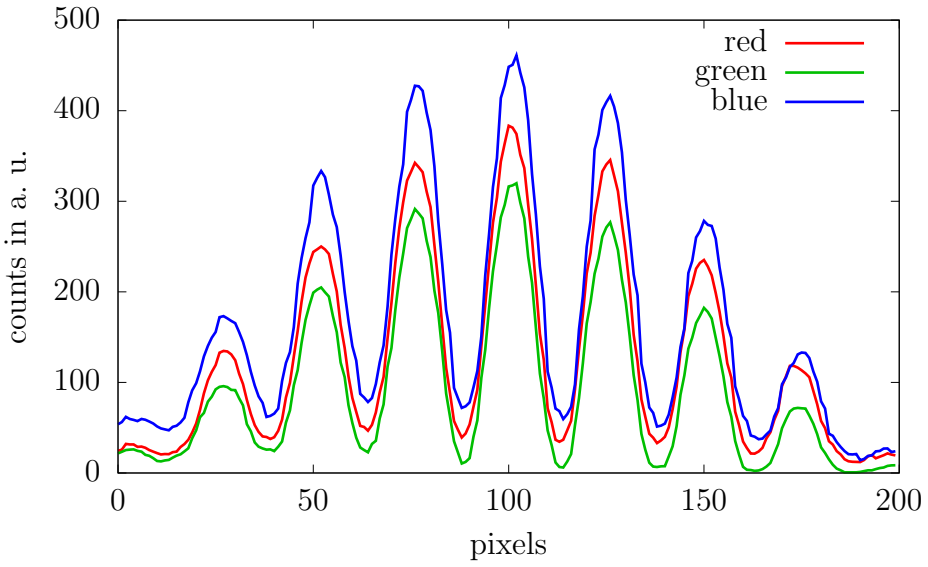

Figure 10: Comparison of the lattice profile measured by the pixels, which are sensitive twos the colours red, green and blue. Contrary to expectations the highest intensity is measured by the pixel which are most sensitiive in the blue region. The green curve shows the best contrast. Therefore further measurements are perform with the data from the green pixels.

Figure 10 shows the intensity profile of the interference pattern with a spacing of 16 µm measured by pixels which are sensitive towards three different colours. The measurement has been done with ISO = 300, an exposure time of 500 µs and at full resolution.

Although the light is in the near-infrared, the blue pixels measure the highest intensity. The green pixels measured the lowest intensity and the curve of the red pixels is in between the other two colours. The data from the green pixels also has the lowest minimal values, which means that the visibility of the green image is the best. For this reason only the data of the green pixels has been evaluated in the following sections of this chapter.

5.3.2 Exposure time and saturation

As already mentioned, the camera chip is expected to show a non-linear response with increasing intensity. Therefore the response of the camera is measured for different exposure times and different laser power. The camera has been set to measure at half of its maximum resolution. The two expressions, shutter time and exposure time, refer to the same setting and are interchangable.

In order to protect the chip against damage from too much laser power, a neutral density filter is placed filter in front of the camera. One of the two parallel beams is blocked, thus only one polarised Gaussian beam is directed at the Pi Camera. The laser power on the chip is further varied by adjusting the $\lambda/2$-waveplate, which determines how much power is transmitted or reflected by the PBS (see figure 9).

Figure 11 shows a measurement of counts depending on the laser power. A Thorlabs NE30A filter is placed in front of the camera. It transmits 0.54 % of the power at 1064 nm [80], so that only a few µW of power reach the camera. For increased laser power the camera's response shows no visible non-linearity for the short exposure time of 200 µs, in contrast the data with the longest exposure time of 1000 µs deviates significantly from linear behaviour. The slope decreases for laser power above 1 µW. This implies a possible saturation effect. As saturation effects are to be avoided, another measurement is performed in a lower power regime.

For the measurements depicted in figure 12 a Thorlabs NE40A filter is used, that only transmits 0.1 % of the power at 1064 nm [80], reducing the incoming laser power from 100 µW to 100 nW. In the range of 200 nW to 600 nW the response is approximately linear, which suggest that there is no saturation. However, no response can be measured below 100 nW.

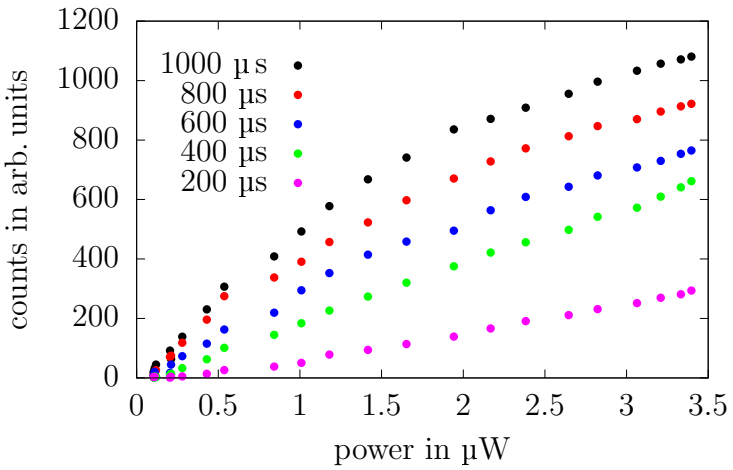

Figure 11: Power measured by the Pi Camera for different exposure times. For the small exposure time of 200 µs, the behaviour is almost linear. For larger exposure times the slope of the curves decreases resulting in non-linearity.

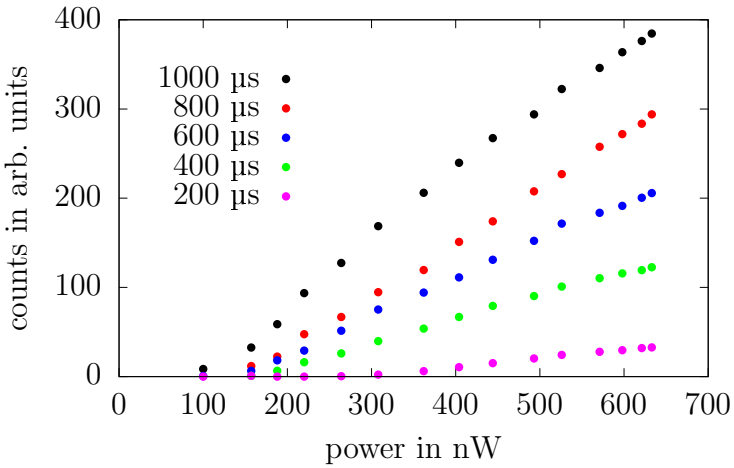

Figure 12: Power measured by the Pi Camera in a low power regime for different exposure times. The camera's response to a power below 700 nW is approximately linear, however, the camera is insensitive beneath 100 nW.

Apart from high laser power, saturation can also occur as a result of a prolonged exposure time. Figure 13 shows how the measured counts increase with exposure time. The measured power increases strongly at small exposure times below 3 ms, after which the slope decreases, indicating saturation.

The effect of saturation on the shape of the measured Gaussian profile is depicted in figure 14. The data is normalised for better comparability of the shape of the curves. For a very short exposure time of 100 µs the curve is very narrow and displays a sharp edge at the base. For longer exposure times the curve slopes off smoothly at the base, as is typical for Gaussian profiles, but it also broadens and becomes flatter at the top. The flattened peak is visible in figure 14 for exposure times of 5 ms and longer, which corresponds to the reduced slope in figure 13. The curve measured with an exposure time of 1 ms has the greatest resemblance with a Gaussian curve. Saturation occurs at exposure times longer than 1 ms.

In conclusion more laser power and longer exposure times cause saturation and enhance the non-linearity of the camera. Reducing both parameters results in a more linear behaviour, but there is also the disadvantage of not being able to measure small intensities, which is why the exposure time should not be set too low.

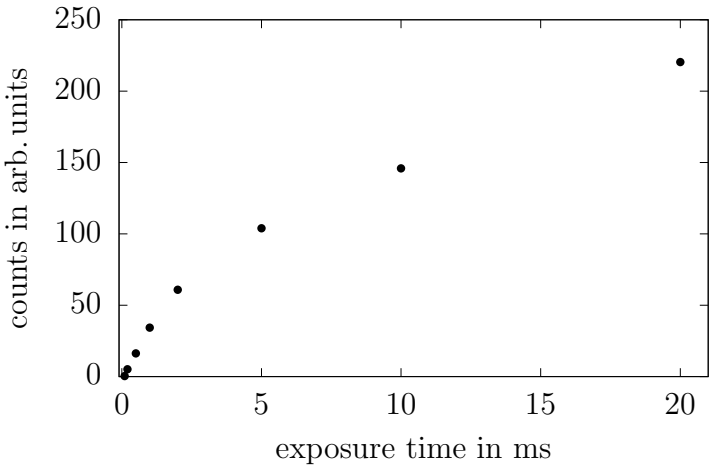

Figure 13: Counts measured at 300 nW for different exposure times ranging from 100 µs to 20 ms. The measured counts increase approximately linearly up to an exposure time of about 2 ms. Thereafter the slope decreases which indicates a saturation effect.

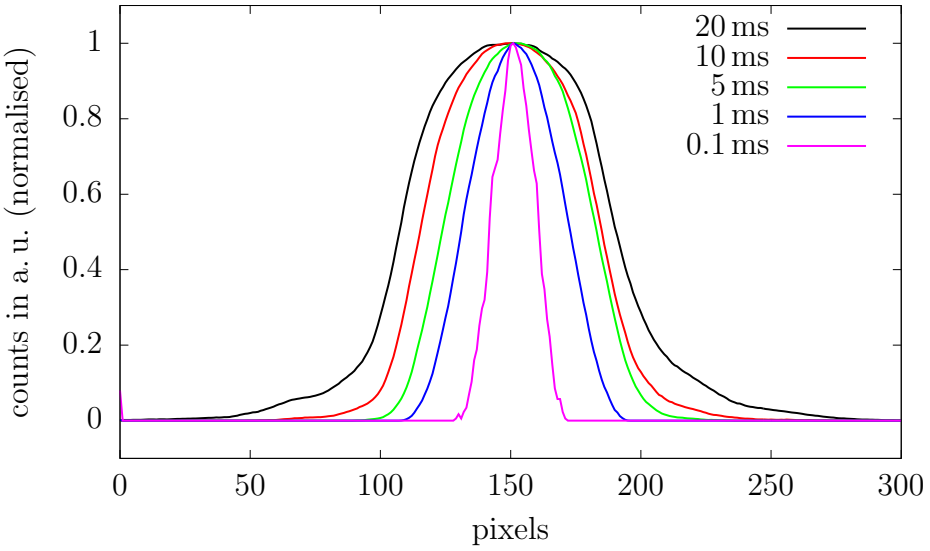

Figure 14: Normalised measurement of a Gaussian profile for different exposure times at 300 nW. For the shortest exposure time the bell curve is significantly reduced in width has an edge at the base instead of sloping off smoothly. For exposure times longer than 5 ms the curve broadens and the top is flattened, which indicates saturation.

5.3.3 Resolution

Apart from settings such as the exposure time for example, the chips finite pixel size has to be taken into account. According to the chip's specifications [86], the pixel size is 1.12 µm x 1.12 µm.

The ratio between the pixel sizes at full, half and a quarter of the maximal resolution hase been measured for different lattice spacings. The pixel diameters for full, half resolution and quarter resolution are expected to be 1.12 µm, 2.24 µm, 4.48 µm, which corresponds to a ratio of 1:2:4, however the measured ratio is 1:3.5:7 and is the same for all pixel colours. This may be due to the binning process performed by the camera. By comparing the measurements with results taken from a beamprofiler with a known pixel size of 3.69 µm x 3.69 µm, the pixel size for each resolution of the Pi Camera can be determined.

Images of an interference pattern with a spacing of approximately 22 µm at different resolutions are depicted in figure 15. All images in figure 15 show an area of 200 µm x 200 µm. The corresponding pixel sizes can be found in table 2. Comparing the values in the table 2 with the expectations shows a match for half and quarter resolution. The pixel size at full resolution is significantly smaller than expected.

Unlike the Pi Camera the beamprofiler has a linear intensity response. Therefore the diameter of the interference pattern measured with the beamprofiler in figure 15a) is visibly larger than in the other pictures taken with the Pi Camera. The beamprofiler is able to measure the small intensities towards the edge of the spot, which are cut off by the Pi Camera. The asymmetry in figure 15a) results from a slight misalignment of the intersecting beams.

The measurement at high resolution depicted in 15b) also shows an interference pattern with small spacing in y-direction. The origin is an interference effect on the camera chip itself or the filters infront of it and does not result from the setup of the accordion lattice. This effect cannot be resolved in the other pictures. The contrast between the bright and dark areas of the lattice is also reduced with resolution, particularly in figure 15d). Also the diameter of the measured image is reduced, which means that the small intensities towards the edge of the lattice are no longer measured.

Taking pictures with higher resolution offers better visibility and allows the measurement of smaller lattice spacings, however it comes at the cost of slower measurment rate. Increasing the resolution also increases the number of pixels that have to be scanned in order to take a picture, which means that each picture takes more time.

Camera	pixel size
Beamprofiler	3.69 µm x 3.69 µm
Pi Camera at full resolution	0.64 µm x 0.64 µm
Pi Camera at half resultion	2.24 µm x 2.24 µm
Pi Camera at quarter resolution	4.48 µm x 4.48 µm

Table 2: Pixel size for different camera resolutions

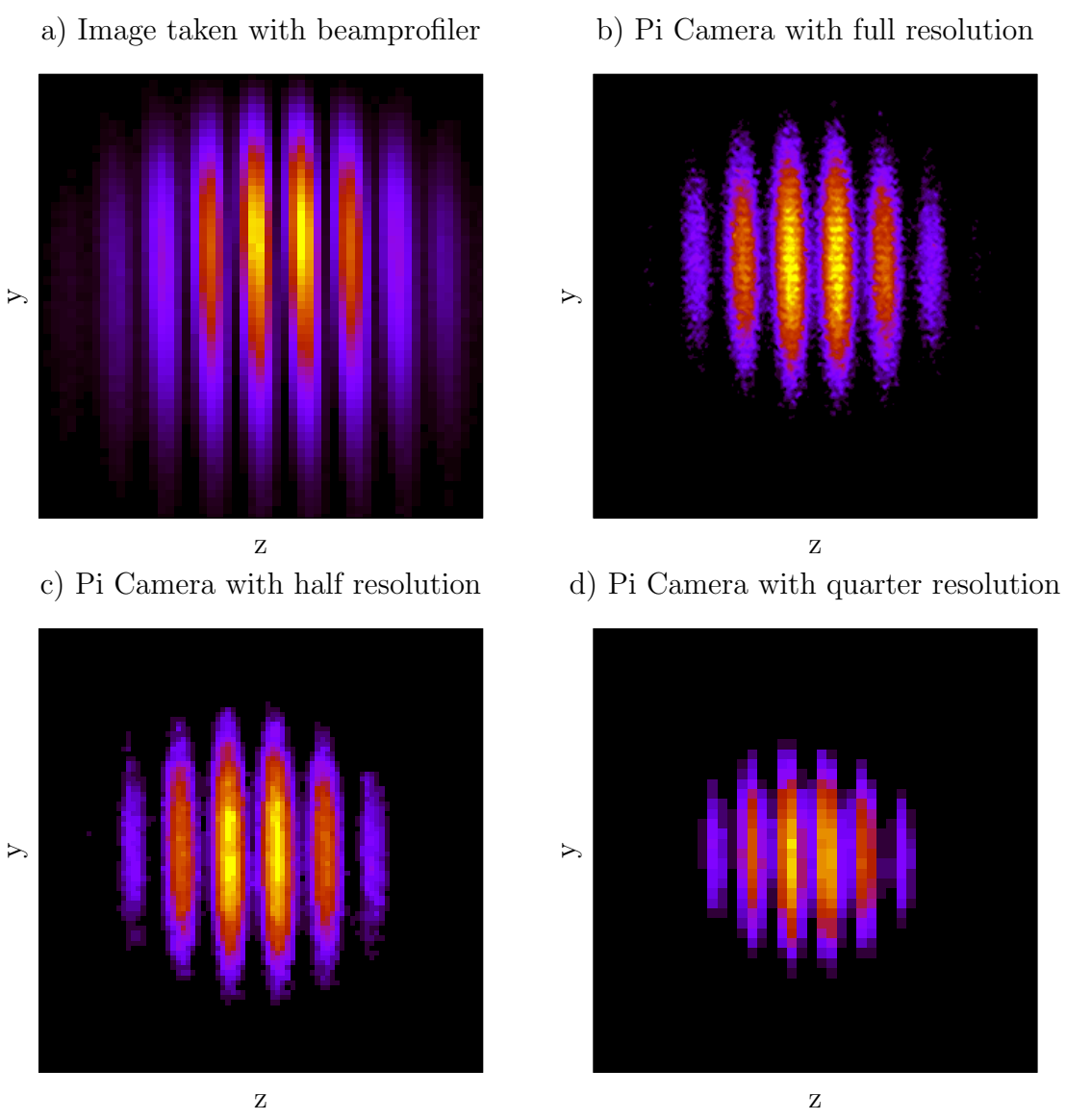

Figure 15: Image of the lattice with a spacing of 22 µm taken with a beamprofiler in a) with a pixel size of 3.69 µm and the Pi Camera at different resolutions with a pixel size of b) 0.64 µm, c) 2.24 µm and d) 4.48 µm.
Each image displays an area of 200 µm x 200 µm.

6 Characterisation of the accordion lattice

This chapter contains measurements of the accordion lattice, including a comparison of the measured lattice spacing with the theoretical expectations. The stability of the position of the intersecting beams has been measured in the focus of the aspheric lens. The phase of the interference pattern during the motion of the mirror was measured, as well as the temperature dependent phase shift in a lattice with static spacing.

6.1 Lattice spacing

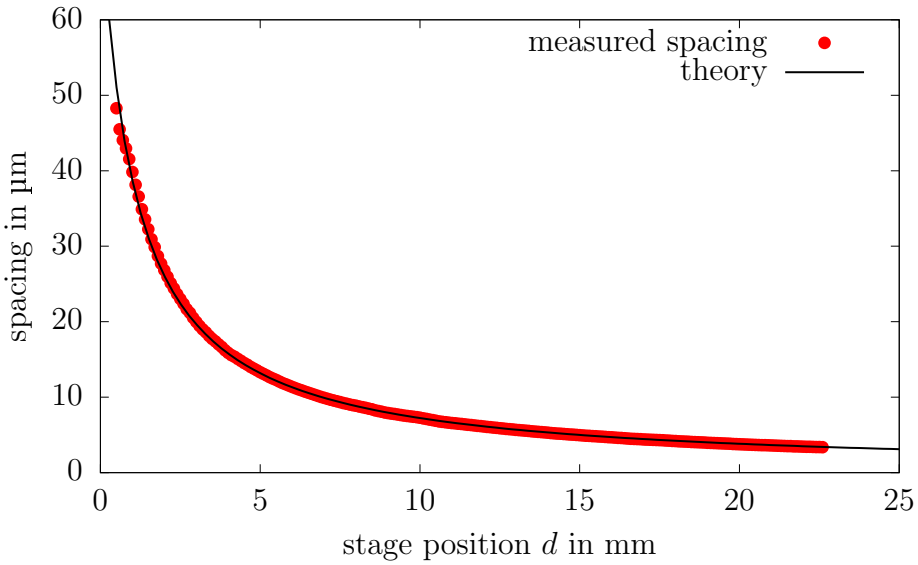

Figure 16: Lattice spacing measured as a function of the stage position d. The bahaviour is in agreement with the theoretical expectation. The data is fitted to equation (77) in order to obtain the offset $d_0 = 1.06$.

Figure 16 shows, how the spacing changes, when the mirror is displaced by the stage. The data is in good agreement with the theoretical expectations given by equation (77). The function has been fit to the data, the offset is determined as $d_0 = 1.06\,\text{mm}$. The spacing ranges from 48.3 µm to 3.37 µm, which corresponds to a distance of $3.3\,\text{mm} \leq \text{D} \leq 47.9\,\text{mm}$ and exceeds the conservative estimate made in chapter 5.2. However for the extremal values of the spacing, parts of the beam started to clip at the edges of the cubes and the mount of the $\lambda/4$-waveplate. The top beam, which is reflected in PBS2 (see figure 9) is clipped earlier than the bottom beam, because it passes through the the $\lambda/4$-waveplate, which is fixed inside a lense tube. The retaining ring, which holds the waveplate in its place, has an aperture of 23 mm. This limits the translation range. For this reason, further measurements are resistricted to a range of $4.58\,\text{mm} \leq \text{D} \leq 46\,\text{mm}$ which corresponds to a spacing range of 3.5 µm to 35 µm.

6.2 Stability during motion of the stage

In an ideal case, the position of the beams and their distance from each other should not vary when the mirror is moved. However this is not the case as measurements in figures 17 and 18 demonstrate. For this measurement one of the parallel beams is blocked and the position of the other beam on the camera is measured while the stage moves. The measurement is then repeated for the other beam. Data outside the range specified in the previous section is omitted due to the clipping of the beam.

Figure 17 shows how the beams move up to 44 µm away from each other along the z-axis.The two curves in figure 17 have almost the same shape, except for the fact that the beams move in opposite directions relative to each other.

Figure 18, which depicts the motion of the beams along the y-axis, shows a parallel behaviour of both beams. The displacement of the beams is almost identical and they deviate less than 10 µm away from each other. Overall the beams move up to 30 µm during the motion of the stage.

The distance between both beams should not be more than half the width of the intersecting beams. The two beams move by $\Delta z = 44$ µm and $\Delta y = 30$, which justifies the beam diameter $w' = 97$ µm in the focal point of the setup. In principle, it is possible to reduce the beamwidth further in y-direction and still achieve a lattice, as the beams only drift up to 10 µm apart along that axis. However, in this case that is not advisable, as the effect of a shift of the whole lattice position is stronger for a smaller spot size.

The measured values Δz and Δy are independent of the speed of the translation stage or the direction in which the stage moves.

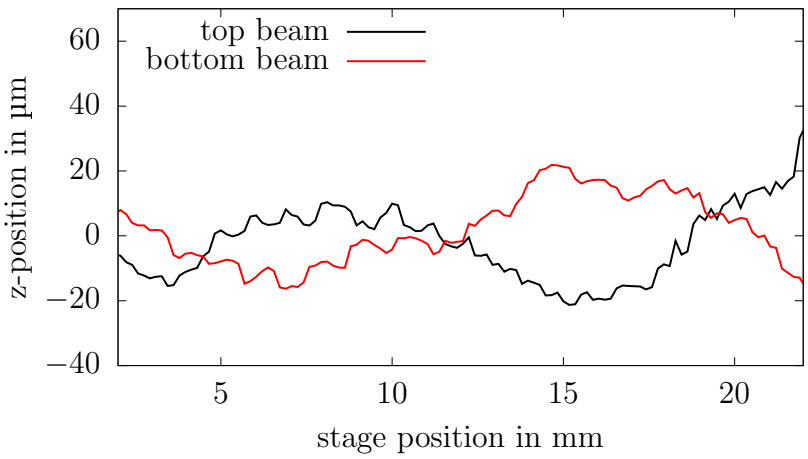

Figure 17: The z position of the two beams on the camera is measured separately during the motion of the translation stage. For a displacement up to 22 mm the two beams move less than 45 µm apart. .

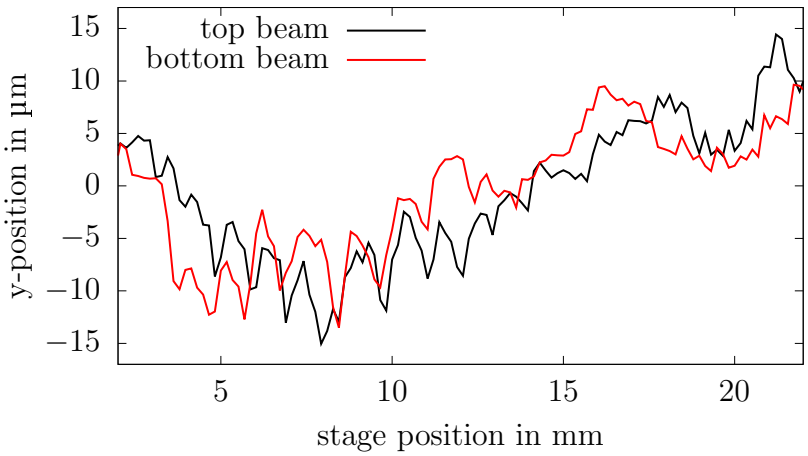

Figure 18: During the motion of the stage both beams move within a range of 30 µm in the focal plane of the aspheric lens. The distance between both beams is less than 10 µm for any stage position.

The speed of the translation stage has no measurable effect on how the fringes of the accordion lattice shift during compression. In figure 19, the lattice spacing has been changed slowly from 35 µm to 3.5 µm within more than two minutes. Afterwards the direction of the stage is reversed and the lattice spacing is reduced at maximum speed within 10 s. The center fringe, which has a maximum at about 60 µm at the beginning of the measurement, moves by 8.6 ± 0.64 µm during compression and during the expansion it moves by 9.0 ± 0.64 µm, which can be considered the same within the margin of error. The uncertainty is defined as one pixel size at full resolution.

During the dispalcement the image of the accordion lattice measured by the Pi Camera becomes darker and brighter. This effect is reapeatable and can be explained by the distance between the intersecting beams during the motion of the stage as well as imperfections of the PBS cubes. However, due to the non-linearity of the Pi Camera, these intensity fluctuations appear magnified in the measurement data.

Although the shift of the center fringe does not depend on the speed or direction of the stage displacement, it is dependent on the alignment of the set up and the temperature. The shift of the center fringe measured at a temperature of 19.7 °C is $z = 8.7$ µm, for 19.9 °C it changes to $z = -8.7$ µm. The change of sign indicates, that the fringe shifts in the opposite direction.

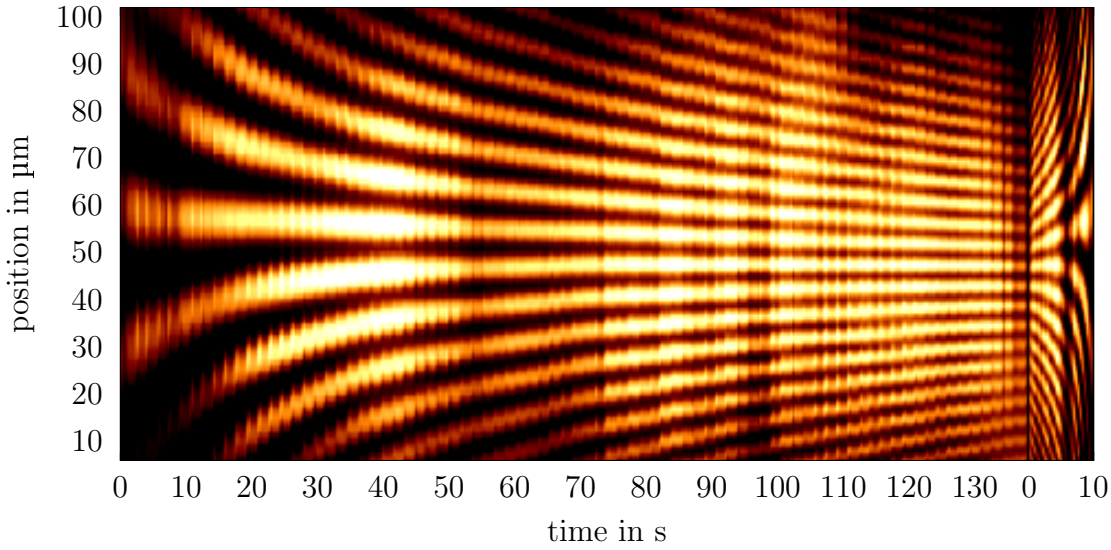

Figure 19: Slow compression of the accordion lattice during a time period of 148 s, followed by a fast expansion of the lattice spacing within 10 s. The center fringe moves by about 9 µm for each direction of motion.

6.3 Temperature stability

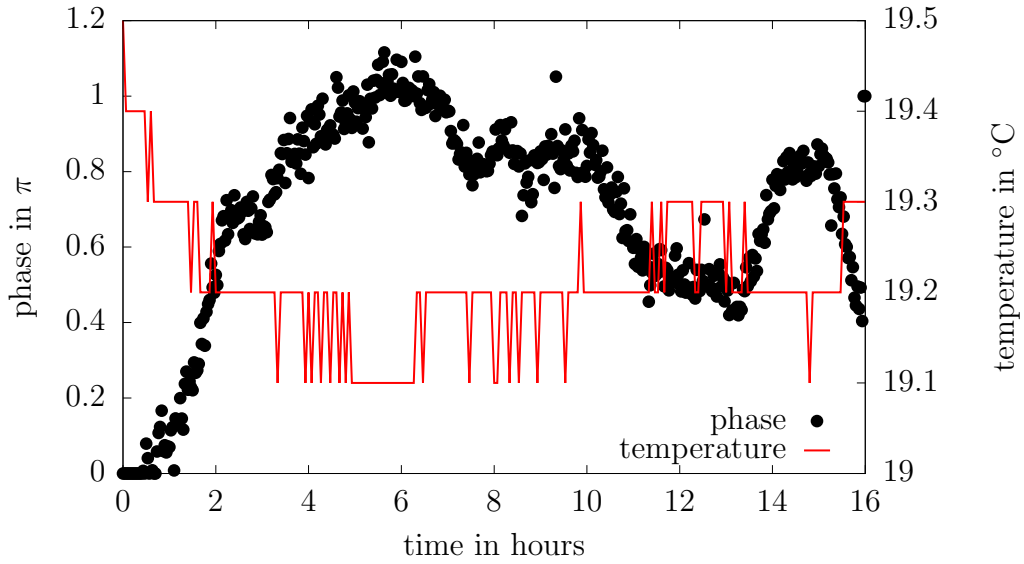

Figure 20: Phase shift (black points) and temperature (red line) measured over the course of 16 hours for a static lattice spacing of 8 µm. The phase was measured every 2 minutes.

The position of the lattice potentials within the Gaussian envelope depends on the phase difference between the two intersecting beams. In an ideal setup the difference in optical pathlength is exactly twice the distance between the surface of PBS1 and the mirror M2 for all distances D. Due to thermal expansion the difference varies with temperature.

In the setup the distance amounts to around 35 mm and the components are mounted on an aluminium breadboard. The thermal expansion coefficient of aluminium is $23.1 \cdot 10^{-6}\,\mathrm{K}^{-1}$ [82]. The setup is therefore expected to have a temperature stability of approximately $3\,\pi/\mathrm{K}$.

Figure 20 shows how the phase and temperature in the laboratory change over the course of 16 hours. The phase is recorded every two minutes and the temperature is measured every four minutes with an accuracy of 0.1 K. A correlation between temperature and phase evolution can be seen: the phase increases with falling temperature and vice versa. For the range of temperature fluctuations in the laboratory, the expansion of the materials can be considered to depend linearly on the temperature. From the data depicted in figure 20, the π-temperature of the system can be calculated, assuming, that the phase behaves linearly with temperature. During the 16 hours, the phase shifts by $\Delta\varphi = 1.12\pi \pm 0.05\pi$ and the temperature difference is $\Delta T = 0.4 \pm 0.1\,\mathrm{K}$. The temperature stability of the system can be calculated to be $\Delta\varphi/\Delta T = 2.8 \pm 0.8\,\pi/\mathrm{K}$, which is close to our first approximation.

To increase passive stability the setup including the aspheric lens has been enclosed in a cardboard box to shield it from major fluctuations in the humidity and temperature. Figure 21 shows the temperature measured simultaneously by two thermometers, one placed inside the box with the setup and one next to the box on the optical table. Over the course of 24 hours the temperature inside the lab has varied by 1 K while the temperature inside the box has changed by 0.5 K. The box has reduced temperature fluctuations by a factor of two.

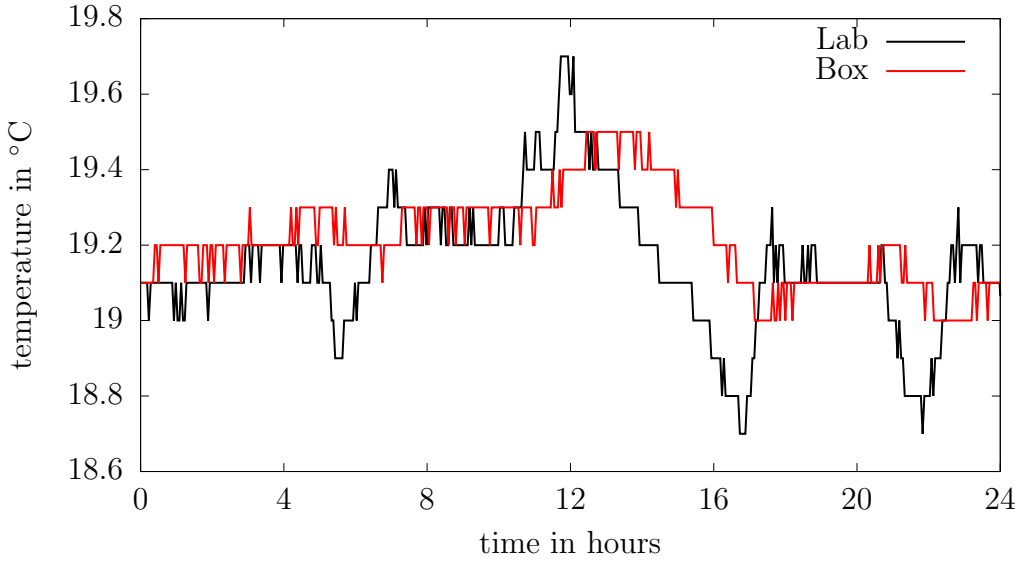

Figure 21: Temperature fluctuations in the lab measured simultaneously inside and outside the box enclosing the setup. The box reduces temperature fluctuations by 50%.

7 Active phase stabilisation

The active phase stabilisation is realised with a feedback loop, that repeatedly measures and corrects the phase. The phase is measured with the Raspberry Pi 3 with an attached Pi Camera. By performing a fourier transformation of the image data from the camera, the phase and spacing of the lattice can be determined. The phase error is measured relative to a position on the camera chip. A voltage output has to be generated and applied to the piezo stack in order to compensate the error.

7.1 Telescope

To avoid the atoms drifting out of the imaging plane the phase of the interference pattern has to remain as stable as possible. This can be achieved by implementing a feedback loop. The phase information can be obtained via a camera and converted into a voltage signal which is applied to the piezo stack shown in figure 9. The camera can however not be placed in the focus of the setup, as this space is already occupied by the cold atoms in the science chamber.

Instead the camera is placed in the focus of an optical telescope in Kepler-configuration, that magnifies the interference pattern. A schematic of the telescope can be found in figure 22. The variables f_1, f_2 and f_3 are the focal lengths of the lenses L1, L2 and L3. The distance between L2 and L3 is arbitrary.

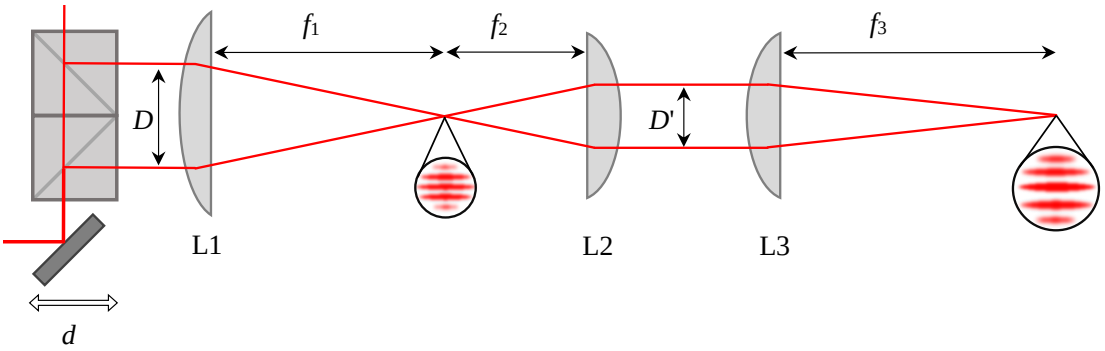

Figure 22: Schematic setup of the telescope in Kepler configuration

The lattice spacing in the focal plane of the telescope is

$$s' = \frac{\lambda}{2}\sqrt{1 + \left(\frac{2f_3}{D'}\right)^2} \tag{79}$$

D' is the distance between the parallel beams between L2 and L3. The distance D' is defined as

$$D' = \frac{f_2}{f_1} D. \tag{80}$$

Inserting equation (80) into equation (81) leads to

$$s' = \frac{\lambda}{2}\sqrt{1+\left(\frac{2f_1}{D}\frac{f_3}{f_2}\right)^2} = \frac{\lambda}{2}\sqrt{1+\left(A\frac{2f_1}{D}\right)^2}. \tag{81}$$

$A = f_3/f_2$ is the magnification of the telescope.

In this case $\left(\frac{2f_1}{D}\right)^2 \gg 1$ is valid, meaning that the following approximation can be made

$$s' \approx A \cdot \frac{\lambda}{2} \cdot \frac{2f_1}{D} = A \cdot s \tag{82}$$

Figure 23 shows the lattice spacing in the focal plane of the telescope as a function of the stage position d. It is very similar to the measurement in the focal plane of the lattice setup depicted in figure 16. The magnification of the telescope can be determined accurately by fitting the data in figure 23 to equation (82). The result is $A = 1.83$. The working distances of the lenses L2 and L3 are estimated to be 7.5 cm and 15.5 cm.

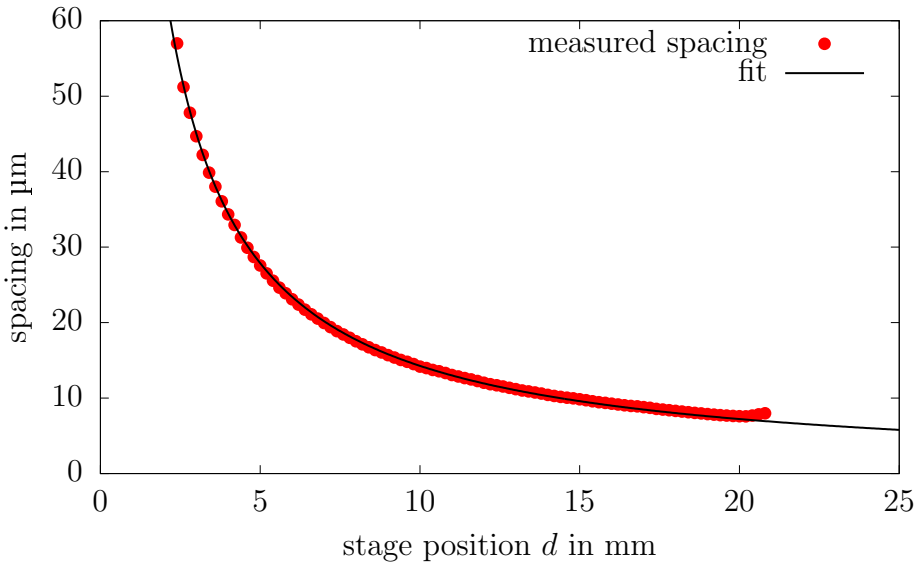

Figure 23: Magnified lattice spacing measured as a function of stage position d. The telescope in Kepler configuration has a magnification of A=1.83.

7.2 Feedback loop

The Raspberry Pi is not capable of creating an analogue voltage output. It can only imitate different voltages via pulse width modulation (PWM). It creates a digital signal which alternates between high (5 V) and low (0 V) at a high frequency (in the range of MHz). The duty cycle refers to the proportion of time spent on the high voltage level within a period. While PWM is sufficient for dimming the light of an led for example, it may not be appropriate for operating a piezo stack.

The piezo stack expands according to the voltage applied to it. The applied voltage has to be an analogue DC signal, since an oscillating voltage signal could also cause an oscillating phase or even damage the piezo if the resonance frequency of the piezo is applied. Therefore, a digital to analogue converter (DAC) is used in order to generate a genuine analogue signal. A high-precision AD/DA board from Waveshare was mounted on top of the Raspberry Pi, which allows for an analogue voltage output within a range of 5 V.

As the voltage range provided by the Raspberry Pi is insufficient to compensate phase errors due to drifting temperature over the course of several hours, an amplifying circuit is added, that enlarges the voltage range to 14.7 V. The amplification circuit also includes a low-pass filter, that removes high frequency noise and protects the piezo. Without the filter the piezo starts buzzing when the amplified voltage is applied, presumably due to a signal close to the piezo's resonance. The piezo used for this setup is a P-080 PICMA stack ring actuator with a resonance frequency between 10 kHz and 20 kHz. The low pass filter has a cutoff frequency of about 800 Hz, which is considerably lower than the resonance and removes most of the noise spectrum.

Figure 24 shows how the phase can be corrected by applying a voltage signal to the piezo. Exemplary, a triangular voltage between 0 V and 14.7 V was applied. The response is also a triangular signal. This implies that the phase responds to the voltage signal in a linear fashion, and in consequence also that the expansion of the piezo is linear with the applied voltage. This linear behaviour is only expected to hold within a relatively low voltage regime. The piezo stack can be operated in a voltage regime of -20 to 100 V. Scanning larger phase differences by applying a larger voltage range may result in non-linearity and a small hysteresis, as is typical for piezos.

Under ideal circumstances the phase shift should be the same for every lattice spacing.Figure 25 shows that the maximal phase that can be shifted with 14.7 V is different for different lattice spacings (or stage positions). There is an almost linear behaviour of the maximal phase shift compared to the stage position. However the difference between the largest phase shift of $4.34\,\pi$ and the smallest phase of $4.07\,\pi$ is only 6 %. The dependence of the maximal phase shift on the lattice spacing is very weak and can be neglected, especially if a measurement error of one pixel is taken into account and because they have no measurable impact on the phase stabilisation with the PID, meaning the phase can be stabilised equally well at all lattice spacings, if the error is measured accurately.

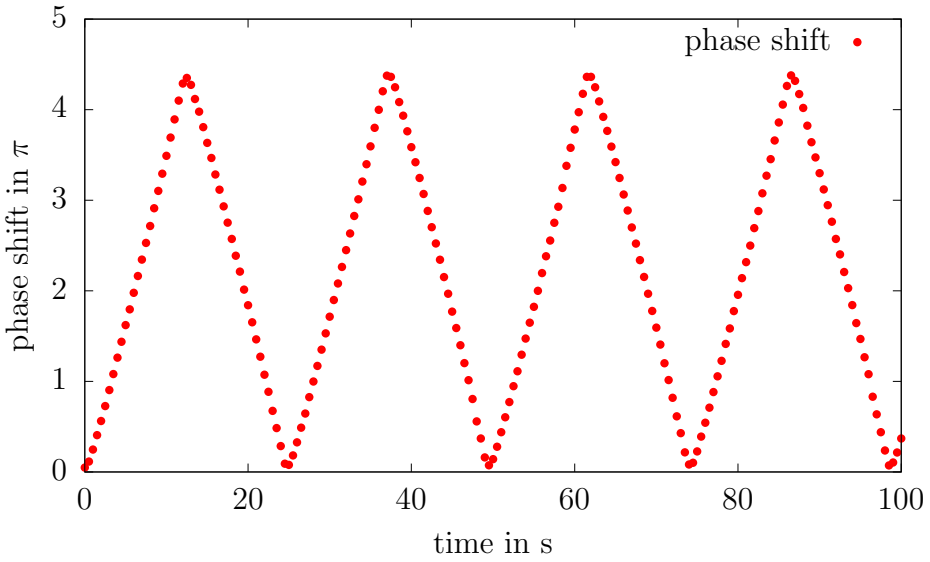

Figure 24: Phase shift measured in the focal plane of the accordion lattice setup at a static spacing of 3.6 µm. A triangular voltage between 0 V and 14.7 V is applied to the piezostack at the back of mirror M2. The phase varies up to 4.34 π.

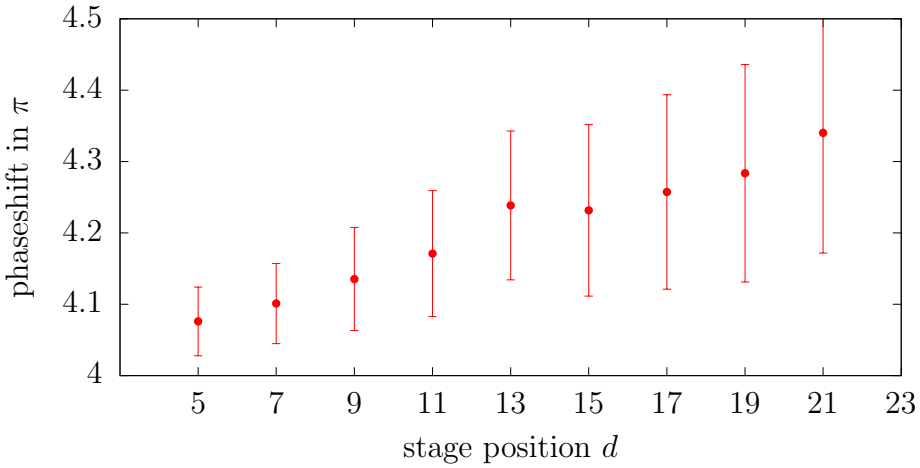

Figure 25: Maximal phase shift in the focal plane of the accordion lattice setup at different stage positions for an applied voltage of 14.7 V. The errorbars result from assuming an error of one pixel in the spacing.

In order to be able to realiably stabilise the atoms in the cold atoms experiment, the phase in the focal plane of the telescope needs to be identical to the phase in the focus of the accordion lattice setup. This is verified by comparing the phase shift in the focal plane of the lattice setup with the phase shift behind the telescope. Figure 26 shows that the phase shift is indeed identical, except for the fact, that it shifts in opposite directions, because the telescope turns the image of the lattice upside down.

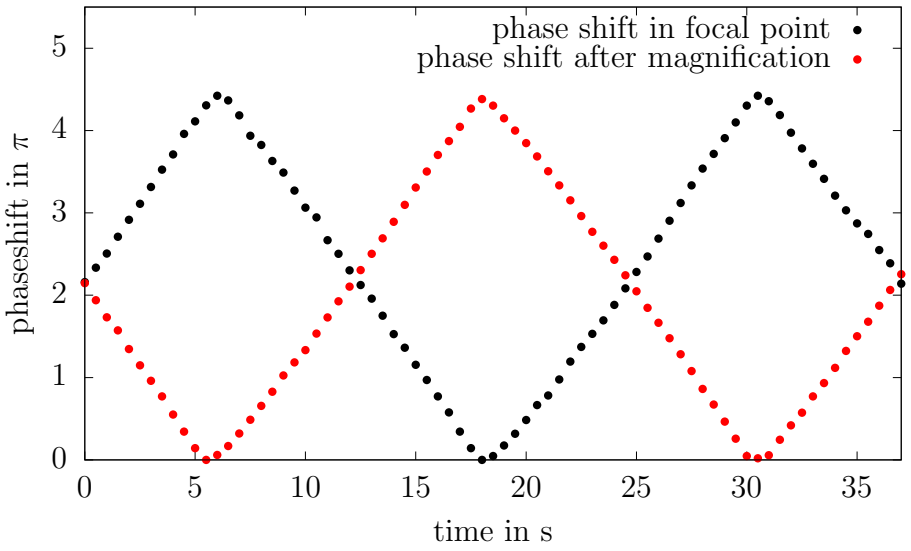

Figure 26: Phase shift measured in the focal plane of the aspheric lens (black data) and in the focal plane of the telescope (red data) for the same stage position. The range of the phase shift is identical with $4.4\,\pi$. The telescope turns the image of the lattice upside down, which causes the phase to shift in the opposite direction. Therefore, the phase error, which can be corrected with a PID, has a different sign behind the telescope.

The phase is measured by integrating the data gathered by the camera along the z-axis. The phase information is obtained by performing a fourier transformation on the data. A proportional-integral-derivative (PID) controller is included into the python code in order to allow active phase stabilisation.

A PID controller is the standard tool for feedback control systems. It repeatedly measures the value, in our case the phase, compares it to a set point, and generates a signal according to the error, that has been measured. The PID controller comprises of three different components. The proportional component (P) generates a signal which is proportional to the error. Without the additional integral (I-) component the system can have a so-called steady state error, which means that it is stabilised at a value which is different from the set point. The I-component also reduces the time the system needs to reach the set point. The derivative (D-) term determines the slope of the error. It dampens the output signal and thereby increases the stability of the system and reduces a possible overshoot of the output. Controllers don't necessarily have to have all of these three components. For some applications, a PI- controller or P-controller is enough. The gain values and cutoff

frequencies of the P-, I- and D- components depend strongly on the system which is to be stabilised.

PID controllers are mostly realised as an electronic circuit, where the input value is a voltage. In this work, however, the controller has been implemented as part of the code. Therefore the measurement of the phase as well as the calculation of the output voltage signal is executed by the same code. A simulated PID is usually slower than its hardware counterpart. However, in our case, the bandwidth of the feedback loop is limited by the Raspberry Pi, which, depending on the amount of data from the camera it has to process, can only handle between 1.5 and 4 phase measurements per second. A PID controller with a bandwidth on the order of kHz for example would not make any significant difference in increasing the bandwidth of the whole feedback system.

Thermal fluctuations usually cause phase drifts on a time scale of minutes and hours. In addition, the phase measurements of the static lattice show a lot of high frequency fluctuations. This could be a consequence of the limited accuracy of the measurement device. Figure 27 shows two stabilised measurements of the phase over the course of 12 hours. One of the stabilisation mechanisms takes the high frequency noise into account, by setting error values below a certain limit to zero. The data of that measurement is depicted in black and the limit is set to $0.1\,\pi$. Fluctuations and drifts below this value are not corrected. The other code generates an output signal for all error values and thereby suffers from the imperfection in the measurement of the phase. The corresponding measurement data is depicted in red.

Looking at figure 27, one can see that both methods stabilise the phase around zero. However, the red data deviates visibly further from the set point than the black data. Its standard deviation is $0.055\,\pi$. For comparison, the standard deviation of the black data is $0.040\,\pi$, which is almost a third less. This difference in stability can also be visualised in an Allan plot.

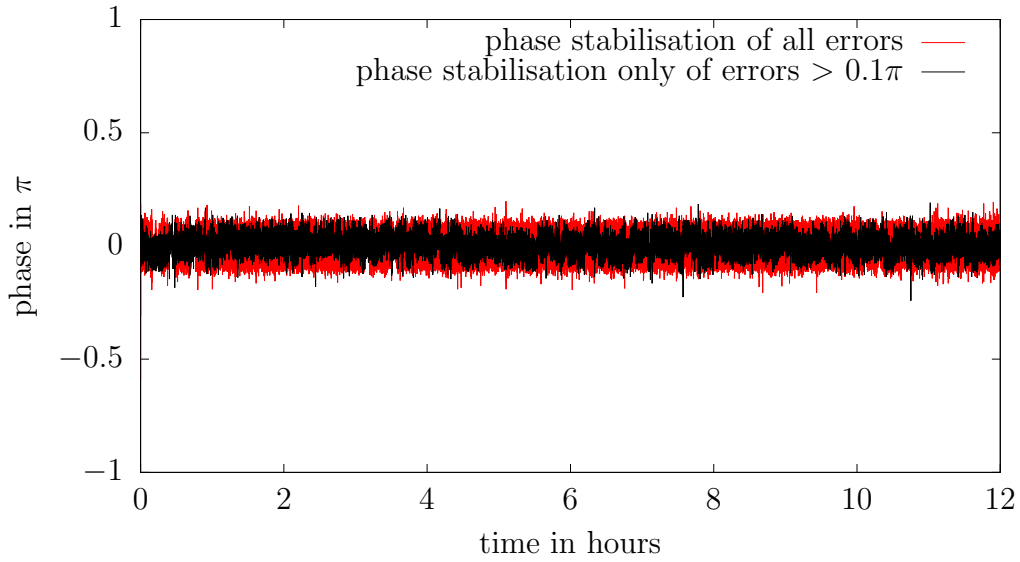

Figure 27: Comparison between two stabilised measurements of the phase. In both measurements the phase was stabilised at the set point of 0. The red measurement data is taken from a phase stabilisation that generates a signal for all measured errors, thereby amplifying the effects of high frequency noise and measurement instabilities. The PID used for the stabilisation of the black data only corrected phase error larger than $0.1\,\pi$. Therefore, the black phase signal is more stable, which is reflected in the smaller standard deviation.

Allan variance or Allan deviation [83] is often used to visualize the stability of a system over time. It can be used to characterise the stability or clocks, gyroscopes of lasers, to name a few examples.

The Allan variance is also known as two-sample variance[83]. It is defined as

$$\sigma^2(\tau) = \frac{1}{2\tau^2}\langle(x_{n+2} - 2x_{n+1} + x_n)^2\rangle. \tag{83}$$

with τ being the sample period, x_n is a phase angle in radians and τ is the sample period. In the case of the accordion lattice x_n corresponds to the measured phase error. The range of the sampling time τ is limited by the measurement rate and the time span of the entire measurement series. The Allan deviation is determined by the square root of the Allan variance [83]

$$\sigma(\tau) = \sqrt{\sigma^2(\tau)}. \tag{84}$$

Graphs, such as the one presented in figure 28, show the stability of a system for different timescales. Usually the Allan deviation becomes smaller for increasing sampling time τ, as the fluctuations with high frequency are averaged out. For very large time scales, the Allan deviation can increase again, as long term drifts, such as for example the temperature fluctuations over the course of one day, take effect. The measurement data in figure 28 show the characteristic decrease of the Allan deviation over time. The lower the value of the Allan deviation for a given

timescale, the higher the stability of the system on that timescale. As is evident from figure 28, the measurement data concerning the phase stabilisation with all error values (black) is consistently higher than that of the phase stabilisation, that neglects the small errors below $0.1\,\pi$ (red). By attempting to correct the high frequency noise, the PID code has amplified the short term fluctuations and reduced stability, even compared to the measurement without active stabilisation, which is depicted in blue. For the timescale of several minutes, a passive system shows less deviation than a imperfectly stabilised one. However on the time scale of hours (10^4 s), both actively stabilised systems are superior to the passive system. The reduced stability of the passive system on that timescale is most likely due to the temperature drifts, which have already been shown to evolve over the course of hours (see figure 21).

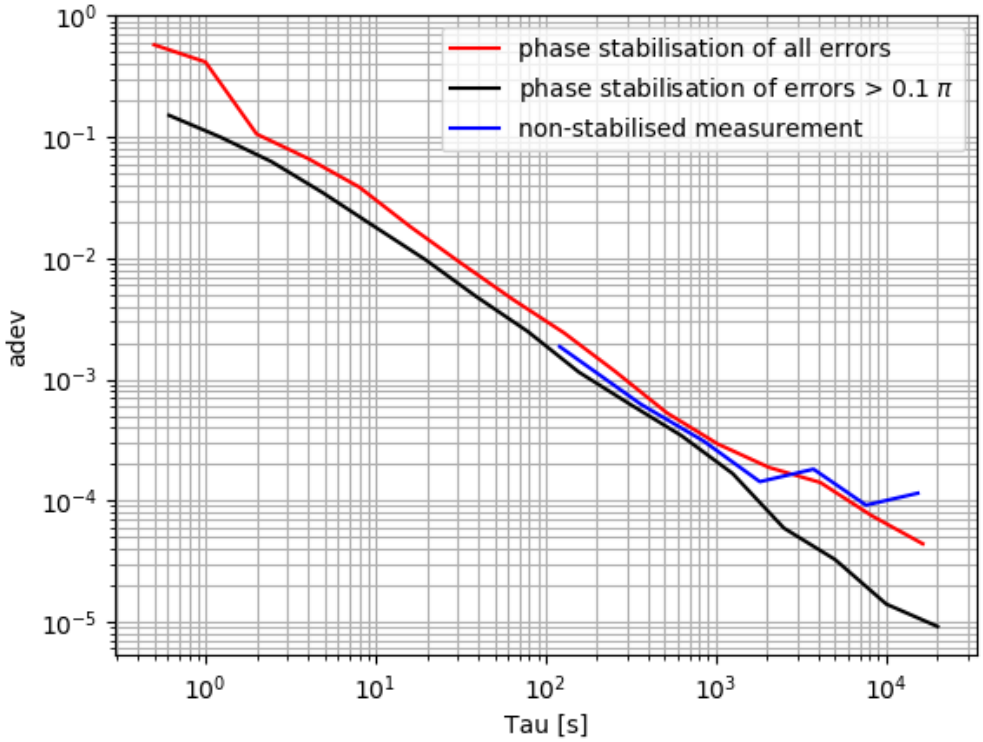

Figure 28: Allan variance for the non-stabilised measurement of the phase depicted in figure 20 in red and black and of the stabilised measurements in figure 27. The stabilised phase has been measured with a rate of 2 Hz, the non-stabilised phase, depicted in blue, was measured every 2 minutes. Therefore the data range of the non-stabilised measurement is much smaller. The red line indicates the stabilised phase, with amplified fluctuations due to the error componsation by the PID. Therefore the Allan deviation is higher than both the other stabilised measurement and the passive measurement up to a sampling time of about an hour. For time scales longer than an hour the temperature drifts register in the data of the passive measurement by increasing the Allan deviation.

8 The accordion lattice as a dipole trap

The accordion lattice is designed to trap ultracold ^{87}Rb atoms with a 1064 nm laser beam. In chapters 6 and 7, the technical details of the accordion lattice were characterised without regard to its purpose as a dipole trap. As there are no measurements of trapped atoms in this thesis, this chapter contains estimations concerning for instance trapping frequencies based on typical experimental values, like for example a trap depth of $k_B \cdot 10\,\mu\text{K}$. All data concerning ^{87}Rb are taken from a table of literature values [84].

8.1 Trapping potential

Like all alkali atoms, ^{87}Rb has a characteristic fine-structure splitting of the D-line. If the detuning of the laser is much larger than the splitting, the fine-structure can be neglected and an effective resonance frequency ω_{eff} is assumed to be in between those two transitions. For linear polarisation the lines of the fine-structure are attributed with strength factors. The line strength factor of the D_1 line is 1/3, for the D_2 line, it is 2/3 [50]. The effective resonance frequency can thus be calculated

$$\omega_{\text{eff}} = \frac{1}{3}\omega_1 + \frac{2}{3}\omega_2. \tag{85}$$

The effective scattering rate can be determined in a similar fashion

$$\Gamma_{\text{eff}} = \frac{1}{3}\Gamma_1 + \frac{2}{3}\Gamma_2. \tag{86}$$

The indices in equations (85) and (86) indicate the data concerning the D_1 and D_2 line. In the case of ^{87}Rb the D_1 transition is $5^2S_{1/2} \rightarrow 5^2P_{1/2}$ and the D_2 transition is $5^2S_{1/2} \rightarrow 5^2P_{3/2}$. The literature values for these transitions are:

$$\begin{aligned}
\omega_1 &= 2\pi \cdot 377.107\,\text{THz} \\
\Gamma_1 &= 2\pi \cdot 5.750\,\text{MHz} \\
\omega_2 &= 2\pi \cdot 384.230\,\text{THz} \\
\Gamma_2 &= 2\pi \cdot 6.066\,\text{MHz},
\end{aligned}$$

which leads to $\omega_{\text{eff}} = 2\pi \cdot 382\,\text{THz}$ and $\Gamma_{\text{eff}} = 2\pi \cdot 6\,\text{MHz}$. The fine-structure splitting is $\Delta'_{\text{FS}} = 2\pi \cdot 7\,\text{THz}$, which is a lot smaller than the detuning of the 1064 nm laser beam at $\Delta = 2\pi \cdot 100\,\text{THz}$. Therefore the fine-structure can be neglected and the atom is considered a two-level system. Equation (45) is valid in this case with some modifications.

$$U_{dipole}(\vec{r}) = -\frac{3\pi c^2}{2\omega_{\text{eff}}^3}\left(\frac{\Gamma_{\text{eff}}}{\omega_{\text{eff}} - \omega} + \frac{\Gamma_{\text{eff}}}{\omega_{\text{eff}} + \omega}\right) I(\vec{r}), \tag{87}$$

Using equation (87), the intensity and the power necessary to reach a certain potential depth can be calculated. The maximum intensity in the center of the accordion lattice can be written as

$$I_{\max} = U_0 \cdot \frac{2\omega_{\text{eff}}^3}{3\pi c^2} \Big/ \left(\frac{\Gamma_{\text{eff}}}{\omega_{\text{eff}} - \omega} + \frac{\Gamma_{\text{eff}}}{.}\omega_{\text{eff}} + \omega\right) \tag{88}$$

Assuming a potential depth of $U_0 = k_B \cdot 10\,\mu\text{K}$, this results in an intensity peak of $I_{\max} \approx 6500\,\text{J/cm}^2$. The intensity profile of the accordion lattice is a sinusoidal function with a spacing s in z-direction and a Gaussian envelope in radial direction. It can be written as

$$I(y,z) = I_{\max} \cdot \cos^2\left(\frac{\pi z}{s} + \frac{\varphi}{2}\right) \cdot \exp\left(-\frac{2(y^2+z^2)}{w^2}\right). \tag{89}$$

φ is the phase of the lattice relative to the center of the Gaussian profile. In our case the width of the Gaussian envelope is $w = 97\,\mu\text{m}$. The power can be calculated by integrating the intensity $I(\vec{r})$ over the lattice area

$$P = \iint dydz\; I(\vec{r}) \tag{90}$$

For small lattice spacings compared to the width of the Gaussian envelope, the following approximation can be made:

$$P \approx \pi w^2 I_{\max}/4. \tag{91}$$

In order to achieve a potential depth of $U_0 = k_B \cdot 10\,\mu\text{K}$, a power of at least $P = 0.485\,\text{W}$ is necessary.

The potential of the accordion lattice along the z-axis is sinusoidal with a Gaussian envelope. Due to the orientation of the lattice the gravity potential has to be taken into account as well, which results in the following potential:

$$U(\vec{r}) = -\frac{3\pi c^2}{2\omega_{\text{eff}}^3}\left(\frac{\Gamma_{\text{eff}}}{\omega_{\text{eff}} - \omega} + \frac{\Gamma_{\text{eff}}}{\omega_{\text{eff}} + \omega}\right) I(\vec{r}) - mgz \tag{92}$$

The potential along the z-axis is defined as

$$U(z) = -U_0 \cdot \cos^2\left(\frac{\pi z}{s}\right) \cdot \exp\left(-\frac{r^2}{w^2}\right) - mgz. \tag{93}$$

The last term accounts for the gravity potential, g is the gravitational acceleration and $m = 1.443160 \cdot 10^{-25}\,\text{kg}$ is the mass of a ^{87}Rb atom.

The potential depth determines the temperature limit for the trapped atoms. Atoms that have a higher thermal energy than the potential depth will leave the trap. The gravitational potential effectively reduces the potential depth by

$$\Delta U_0 = mgs/2. \tag{94}$$

This means that the effect of gravity on a particle in a single potential well is reduced for small spacing.

For the maximum spacing of $s = 35\,\mu\text{m}$, this potential reduction equals $\Delta U_0/k_B = 1.78\,\mu\text{K}$ in all potential wells. In consequence, the potential depth of lattice sites, which are further from the center of the Gaussian envelope, is significantly reduced. In the example of a lattice with maximal spacing, a lattice site, which is 78 µm displaced from the lattice center along the z-axis, only has a trap depth of 1 µK. Without the gravity potential the same potential depth is found at a 104 µm. At 90 µm, gravity reduces the effective potential depth to zero.

For a spacing of 3.5 µm, the effect of the gravity potential is only $\Delta U_0/k_B = 178\,\text{nK}$ and the potential depth of a lattice site becomes zero at 137 µm distance from the lattice center. Figure 29 shows the lattice potentials with two different lattice spacings.

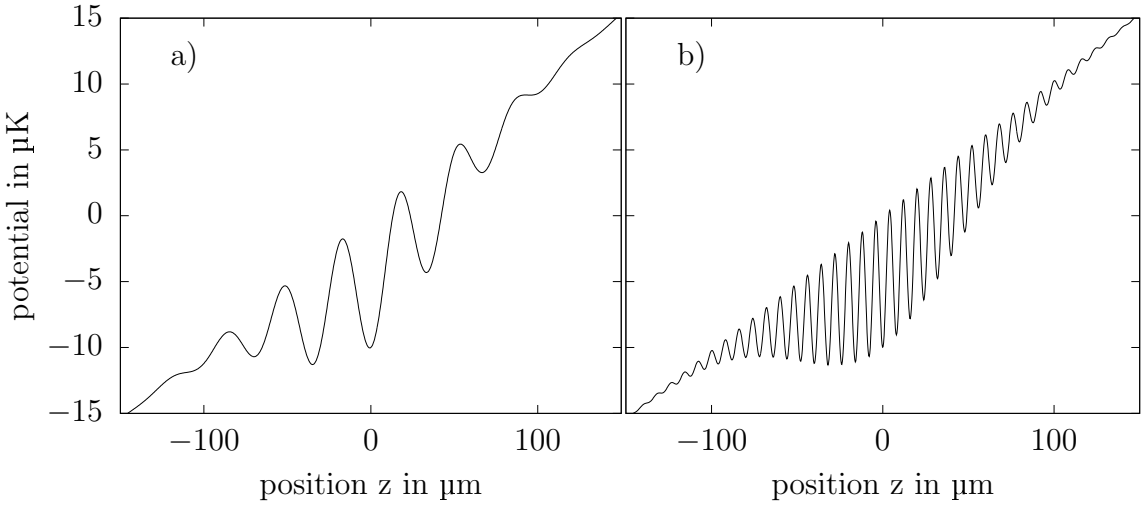

Figure 29: Comparison of the lattice trapping potential for ^{87}Rb atom with a large spacing of a) $s = 35\,\mu m$ and with smaller spacing b) $s = 8\,\mu m$. The effective potential depth of the individual lattice sites is reduced by the gravitational potential, which is taken into account as a linear slope. This effect is stronger for large lattice spacing and becomes negligible at very small spacing.

8.2 Trapping frequencies

Dipole traps with deep trapping potentials ($U_0 \gg E_R$) are often characterised by their trapping frequency, which is calculated by approximating the shape of the individual potential wells with a harmonic potential. As this approximation only takes the curvature of the potential into account, additional linear terms, such as the gravity potential are neglected, provided of course, that the effective depth is still significantly larger than the recoil energy. In the case of the accordion lattice, the atoms are loaded into a single plane and the lattice spacing is then decreased by moving the mirror on the stage by a distance d. The trapping frequency changes during the compression of the lattice. The trapping frequency of a potential well in the center of the Gaussian envelope ($\varphi = 0$) is defined as

$$\omega_{tr}(s) = \sqrt{\frac{2U_0}{m}}\,\frac{\pi}{s}. \tag{95}$$

It can also be expressed as a linear function of the stage position d using the approximation in equation (78)

$$\omega_{tr}(d) = \sqrt{\frac{2U_0}{m}}\,\frac{2\pi}{\lambda f}\,d. \tag{96}$$

The offset d_0 is neglected in this example. Assuming that there is no shift of the potential well relative to the center of the Gaussian profile, the trapping frequency has a linear dependence on the stage position.

If the atoms are not loaded into the center of the accordion lattice, then the dependence is no longer linear. The position of the potential well into which the atoms are loaded can be defined as a phase offset φ in radian. Assuming the phase stays constant during compression, the position of the potential well shifts towards the center of the lattice, where the potential is deeper. The trapping frequency can then by written as

$$\begin{aligned}\omega_{tr} =& \sqrt{\frac{2U_0}{m}} \exp\left(-\frac{1}{w^2}\left(\frac{s\varphi}{2\pi}\right)^2\right)\frac{\pi}{s} \\ =& \sqrt{\frac{2U_0}{m}} \exp\left(-\frac{1}{w^2}\left(\frac{\lambda f\varphi}{4\pi d}\right)^2\right)\frac{2\pi}{\lambda f}d.\end{aligned} \tag{97}$$

In the case of $\varphi = 0$, this equation can be reduced to equations (95) and (96). Due to gravity there are no potential wells beyond 90 µm from the lattice center with a maximum spacing of 35 µm, that can trap atoms of finite temperature. This distance corresponds to a phase of $5\,\pi$. Assuming that atoms can still be trapped at a 70 µm, which corresponds to a $4\,\pi$ phase offset, the trapping frequency in that well is about half of the frequency in the center, which is a significant difference. As the lattice is compressed, the difference in trapping frequencies between neighbouring sites is reduced. For offsets within the range of $4\,\pi$ the difference is smaller than 5 % at a lattice spacing of 10 µm, which corresponds to a translation distance of 8 mm on the stage. The trapping frequencies during the compression of the lattice are depicted in figure 30 for different offsets φ.

For the spacing range of the accordion lattice in this thesis the frequency in the center potential well can be tuned in the range of $2\pi\cdot 0.63\ \text{kHz} < \omega < 2\pi\cdot 6.25\,\text{kHz}$. If the atoms were loaded into the trap with a phase offset of $4\,\pi$ the frequency range extends to $2\pi\cdot 0.37\ \text{kHz} < \omega < 2\pi\cdot 6.25\,\text{kHz}$.

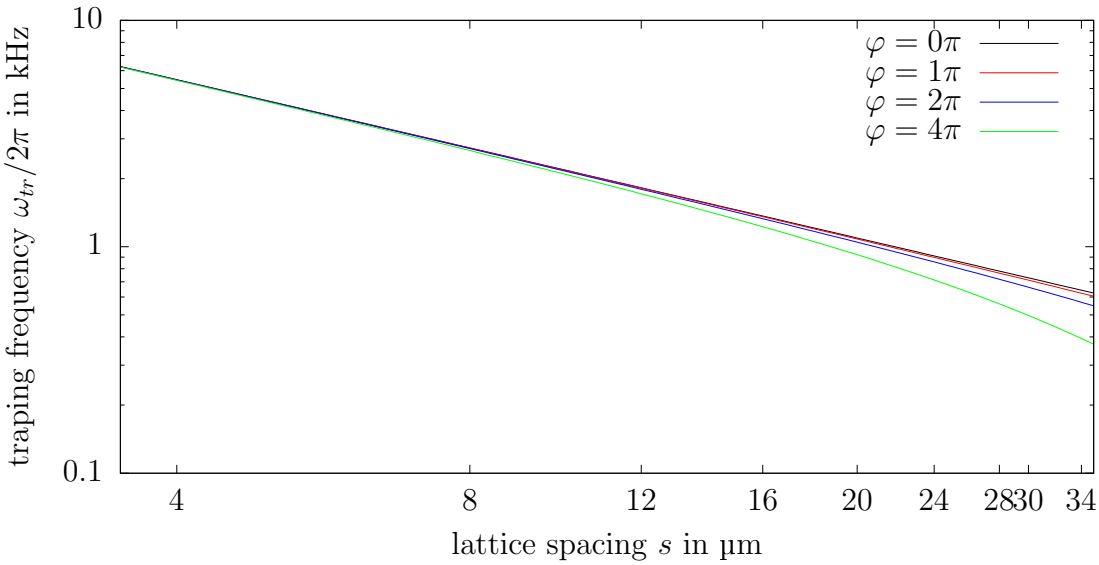

Figure 30: The trapping frequency in the accordion lattice increases as it is compressed to smaller lattice spacings. At large spacing lattice sites which are offset from the center of the lattice have a significantly lower trapping frequencies than the potential well in the center. The offset is defined as a phase offset φ, which in this example remains constant during compression. The offset $\varphi < 4\pi$ can be neglected for lattice spacings smaller than 10 µm.

9 Comparison with other Quasi-2D- dipole traps

There are of course other methods for creating a pancake shaped trapping potential. Further examples are given in the following paragraphs.

One example is the lightsheet already implemented in the experiment, which consists mainly of three lenses, two cylindrical and one spherical. These lenses create an elliptical beam with a very narrow beam waist along one axis, resulting in a pancake shaped trapping potential. The trapping beam has a red detuning relative to the resonance of the atoms, so the dipole force in the trap is attractive. The cold atoms are trapped in the focus of the gaussian beam. With the schematic setup is depicted in figure 31 a waist of around $\omega_z = 10$ µm along the short axis and $\omega_y = 110$ µm along the long axis can be achieved [89].

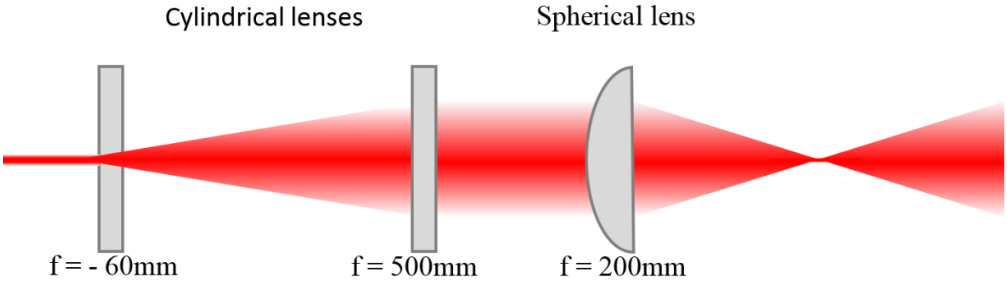

Figure 31: Schematic of the lightsheet. This is an example of a red detuned dipole trap. The beam profile is elliptical due to the cylindrical lenses. The atoms are trapped in the focus of the system with tight confinement perpendicular to the beam.

Another method produces a 2d trapping potential with a single beam of blue detuned light. The laser beam passes through a phase-mask that shifts the phase of the upper half of the beam by π. This creates a first order Hermite-Gauss mode, where the upper and lower half of the beam are separated by a dark line in which the cold atoms are trapped. This offers a few advantages over red-detuned traps. As the atoms are stored in dark areas, side effects through atom-light-interaction, like photon scattering or light shift of the atomic levels, are minimized. The confinement can be tuned either by changing the intensity of the beam or the position of the Hermite-Gauss focus in respect to the trapped atoms. However this kind of tuning also changes the trap depth. A schematic of the setup is depicted in figure 32[87].

It is also possible to load the atoms into a static lattice with small spacing and remove the atoms from all but a single layer with radio frequency radiation. However this procedure requires a high amount of precision for removing excess pancakes and comes with a significant loss of atoms.

The main advantage of the accordion lattice featured in this master thesis is its flexibility. It offers a relatively large range of spacing, in this example between 35 µm and 3.5 µm and allows a high level of control. By being able to control the spacing as well as the phase, one can dynamically tune the confinement and adjust position of the trapped atoms along one axis.

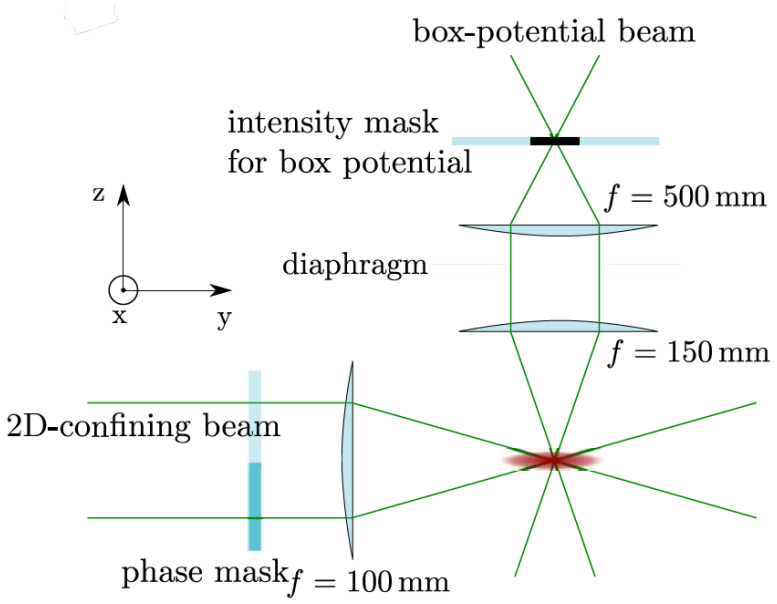

Figure 32: Schematic of the 2d trapping potential using a Hermite-Gauss mode using blue-detuned light. The Hermite-Gauss mode is generated with a phase mask, that shifts the phase of half of the beam. Destructive interference at the border between the two beams results in a dark line, in which the atoms are traped.[87]

10 Conclusion and Outlook

The topic of this thesis is the setup and characterisation of an accordion lattice for the purpose of wave function imaging.

The accordion lattice presented in this thesis is intended to function as a quasi-2D trapping potential for a BEC of ^{87}Rb atoms. The BEC serves as a contrast medium for the visualisation of a Rydberg electron orbital. Therefore the accordion lattice has to provide a spacing range, which allows the loading of a single plane at large spacing, and provide tight confinement for the process of wave function imaging itself.

The accordion lattice presented in this thesis can create a lattice with a variable lattice spacing between 3.5 µm and 35 µm, which fulfills these requirements. Another requirement is that the pancake potential in which the atoms are trapped, stays within the focal depth of the imaging system. This thesis focuses largely on the realisation of the stabilisation in the imaging plane.

A main part of this thesis was setting up the measurement system for gathering and evaluating data on the accordion lattice and implementing a feedback loop. For this purpose a Raspberry Pi3 in combination with a Pi Camera NoIR was chosen. The Raspberry Pi is of advantage, because it is small, inexpensive and at the same time highly versatile, as it can measure data and create different voltage outputs on a number of pins. A pre-existing code, which used a Raspberry Pi as a beamprofiler, was adjusted to suit the measurement requirements. By performing a fourier transformation of the image data from the camera, the phase and spacing of the lattice could be determined. The same code was supplemented to include a PID, thereby generating a voltage signal that, after amplification, regulates the phase with a piezo stack. The Raspberry Pi was also used to trigger the controller of the translation stage to perform predefined motions, such as for example moving the mirror on the stage by one millimeter.

Characterisation measurements of the PiCamera reveal, that the camera has non-linear behaviour and is insensitive to small intensities. However, the camera is sufficient for measuring the lattice spacing and phase.

Contrary to expectations the pixel size of the Pi Camera at maximum resolution was measured at 0.64 µm, instead of 1.12 µm, as is stated in the camera's data sheet. This smaller pixel size allows for resolving the whole spacing range of the accordion lattice in the focus of the aspheric lens.

As mentioned before, the phase was stabilised using a Raspberry Pi for measuring the phase error and generating the output. The phase measurement has a certain amount of noise, which can be amplified by the PID. A more stabile system can be achieved by only correcting phase fluctuations, which exceed the noise.

Even though the current feedback system is effective in correcting phase errors due to temperature fluctuations, additional thermal stability would improve the accordion lattice as a dipole trap for cold atoms. Thermal drifts of the position of the whole lattice for instance cannot be compensated with the piezo. Furthermore the phase shift during the displacement of the mirror is assumed to have temperature dependence. Mounting the components on a material with low thermal expansion, such as for instance titanium [91] and/or additional temperature

stabilisation with a peltier element can improve the stability and thereby facility repeatable measurements with cold atoms.

Furthermore, the Gaussian waist of the accordion lattice is 97 µm and rather large compared to other other existing dipole traps. It is limited by the straightness of the translation stage. Choosing a more advanced translation stage with less deviation, could allow to reduce the size of the trapping beam, especially along the z-axis. A smaller beam waist would mean that the same confinement can be achieved with less laser power. Alternatively, instead of the translation stage, an accousto-optical modulator (AOM) could be used in combination with a lens [92].

List of Figures

Literatur

[1] E. Schrödinger. "Quantisierung als Eigenwertproblem." Annalen der physik 385.13 (1926): 437-490.

[2] A. S. Stodolna, et al. "Hydrogen atoms under magnification: direct observation of the nodal structure of stark states." Physical review letters 110.21 (2013): 213001.

[3] F. Moresco and A. Gourdon. "Scanning tunneling microscopy experiments on single molecular landers." Proceedings of the National Academy of Sciences 102.25 (2005): 8809-8814.

[4] P. Puschnig, et al. "Reconstruction of molecular orbital densities from photoemission data." Science 326.5953 (2009): 702-706.

[5] Karpiuk, Tomasz, et al. "Imaging single Rydberg electrons in a Bose-Einstein condensate," New Journal of Physics **17**, 053046 (2015)

[6] Supplementary information to: Karpiuk, Tomasz, et al. "Imaging single Rydberg electrons in a Bose-Einstein condensate," New Journal of Physics **17**, 053046 (2015)

[7] S. N. Bose, "Plancks Gesetz und Lichtquantenhypothese," Z. Phys., 26, 178–181 (1924).

[8] A. Einstein, "Quantentheorie des einatomigen idealen Gases," Sitzungsberichte der Preußischen Akademie der Wissenschaften, pages 261–267 (1924).

[9] C. J Pethick, H. Smith, "Bose-Einstein Condensation in Dilute Gases" Cambridge University Press (2002)

[10] Dalfovo, Franco, et al. "Theory of Bose-Einstein condensation in trapped gases." Reviews of Modern Physics 71.3 (1999): 463.

[11] M. H. Anderson, et al. "Observation of Bose-Einstein condensation in a dilute atomic vapor." science 269.5221 (1995): 198-201.

[12] K. B. Davis, et al. "Bose-Einstein condensation in a gas of sodium atoms." Physical review letters 75.22 (1995): 3969.

[13] W. Ketterle, D. S. Durfee, and D. M. Stamper-Kurn. "Making, probing and understanding Bose-Einstein condensates." arXiv preprint cond-mat/9904034 (1999).

[14] K. S. Kleinbach, "Ions and Electrons Interacting with Ultracold Atoms -Novel Approaches Based on Rydberg Excitations," PhD thesis, University of Stuttgart (2018)

[15] Damir Zajec, "Stationäre und dynamische Eigenschaften von dipolaren Bose-Einstein-Kondensaten in verschiedenen Fallenpotentialen," PhD thesis, University of Stuttgart (2015)

[16] S. B. Papp, J. M. Pino, and C. E. Wieman. “Tunable miscibility in a dual-species Bose-Einstein condensate.” Physical review letters 101.4 (2008): 040402.

[17] William D. Phillips, “Nobel Lecture: Laser cooling and trapping of neutral atoms.” Reviews of Modern Physics 70.3 (1998): 721.

[18] P. D. Lett, et al. “Optical molasses.” JOSA B 6.11 (1989): 2084-2107.

[19] P. Bouyer and MA Kasevich, “Heisenberg-limited spectroscopy with degenerate Bose-Einstein gases” Phys. Rev. A 56 (1997): R1083.

[20] M. Hiller, et al. ”Characterizing high-n quasi-one-dimensional strontium Rydberg atoms.”Physical Review A 89.2 (2014): 023426.

[21] Yu N. Gnedin et al. “Rydberg atoms in astrophysics.” New astronomy reviews 53.7-10 (2009): 259-265.

[22] J. A. Sedlacek, A. Schwettmann, et al. “Atom-Based Vector Microwave Electrometry Using Rubidium RydbergAtoms in a Vapor Cell.” Phys. Rev. Lett. 111, 063001 (2013)

[23] H. Weimer, M., Müller, et al. “A Rydberg quantum simulator.” Nat. Phys. 6, 382 (2010).

[24] D. Jaksch, J. I. Cirac, et al. “Fast Quantum Gates for Neutral Atoms.” Phys. Rev. Lett. 85, 2208 (2000).

[25] M. D. Lukin, M. Fleischhauer, et al. “Dipole Blockade and Quantum Information Processing in Mesoscopic Atomic Ensembles.” Phys. Rev. Lett. 87, 037901 (2001).

[26] M. Saffman, T. G. Walker,et al. “Quantum information with Rydberg atoms.” Rev. Mod. Phys. 82, 2313 (2010).

[27] M. P. Robinson, B.L. Tolra, et al. “Spontaneous Evolution of Rydberg Atoms into an Ultracold Plasma.” Phys. Rev. Lett. 85, 4466 (2000).

[28] T. Pohl, T. Pattard, et al. “Plasma formation from ultracold Rydberg gases.” Phys. Rev. A 68, 010703 (2003).

[29] M. Müller, A. Kölle et al. “Room-temperature Rydberg single-photon source.” Physical Review A 87.5 (2013): 053412.

[30] T. F. Gallagher, “Rydberg atoms” Cambridge University Press (2005)

[31] Li, Wenhui, et al. “Millimeter-wave spectroscopy of cold Rb Rydberg atoms in a magneto-optical trap: Quantum defects of the ns, np, and nd series.” Physical Review A 67.5 (2003): 052502.

[32] Han, Jianing, et al. “Rb n f quantum defects from millimeter-wave spectroscopy of cold Rb 85 Rydberg atoms.” Physical Review A 74.5 (2006): 054502.

[33] K. Kopitzki, “Einführung in die Festkörperphysik,” Teubner Studienbücher (1993)

[34] M. Marinescu, H. R. Sadeghpour, et al. “Dispersion coefficients for alkali-metal dimers.” Physical Review A 49.2 (1994): 982.

[35] M. L. Zimmerman, et al. “Stark structure of the Rydberg states of alkali-metal atoms.” Physical Review A 20.6 (1979): 2251.

[36] D. Tong, et al. “Local blockade of Rydberg excitation in an ultracold gas.” Physical Review Letters 93.6 (2004): 063001.

[37] D. Barredo, et al. “Demonstration of a strong Rydberg blockade in three-atom systems with anisotropic interactions.” Physical review letters 112.18 (2014): 183002.

[38] J. J. Sakurai, “Modern Quantum Mechanics, Revised Edition.” Am.J. Phys. 63, 93 (1995)

[39] E. Fermi, “Sopra lo spostamento per pressione delle righe elevate delle serie spettrali,” Nuovo Cimento, 11, 157–166 (1934).

[40] Felix Engel, “Ultracold chemistry of a Rydberg atom in a rubidium 87 BEC.” master thesis, University of Stuttgart (2016)

[41] W. F. Holmgren, et al. “Absolute and ratio measurements of the polarizability of Na, K, and Rb with an atom interferometer.” Physical Review A 81.5 (2010): 053607.

[42] I. Beigman and V. Lebedev, “Collision theory of Rydberg atoms with neutral and charged particles,” Physics Reports, 250, 95–328 (1995).

[43] C. Bahrim, U. Thumm, and I. I. Fabrikant. “3Se and 1Se scattering lengths for e-+ Rb, Cs and Fr collisions.” Journal of Physics B: Atomic, Molecular and Optical Physics 34.6 (2001): L195.

[44] M. Schlagmüller, “A single Rydberg Atom interacting with a Dense and Ultracold Gas” PhD thesis, Universtity of Stuttgart (2016)

[45] M. Schlagmüller, T. Liebisch et al. “Probing an electron scattering resonance using Rydberg molecules within a dense and ultracold gas.” Physical review letters 116.5 (2016): 053001.

[46] M. Schlagmüller, et al. “Ultracold chemical reactions of a single Rydberg atom in a dense gas.” Physical Review X 6.3 (2016): 031020.

[47] J. B. Balewski, et al. “Coupling a single electron to a Bose–Einstein condensate.” Nature 502.7473 (2013): 664.

[48] R. Löw, et al. “An experimental and theoretical guide to strongly interacting Rydberg gases.” Journal of Physics B: Atomic, Molecular and Optical Physics 45.11 (2012): 113001.

[49] K. S. Kleinbach, F. Meinert, et al. "Photoassociation of Trilobite Rydberg Molecules via Resonant Spin-Orbit Coupling," Phys. Rev. Lett. **188**, 223001 (2017)

[50] R. Grimm, M. Weidemüller, et al. "Optical dipole traps for neutral atoms," Advances in atomic, molecular and optical physics Vol. 42, 95-170 (2000)

[51] M. Lewenstein, A. Sanpera, et al, "Ultracold atomic gases in optical lattices: Mimicking condensed matter physics and beyond." Adv. Phys **56**, 243-379 (2007)

[52] I. Bloch. "Ultracold quantum gases in optical lattices." Nature Physics 1.1 (2005): 23.

[53] L. Santos, et al. "Atomic quantum gases in kagomé lattices." Physical review letters 93.3 (2004): 030601.

[54] F.H.L. Essler, H. Frahm, et al. " The One-Dimensional Hubbard Model," Cambridge University Press, Cambridge (2005)

[55] D. Jaksch, P. Zoller. "The cold atom Hubbard toolbox." Annals of physics 315.1 (2005): 52-79.

[56] T. Claeson and P. Delsing (Eds), Condensation and Coherence in Condensed Matter, Proc. of the Nobel Jubilee Symposium, Göteborg 2001 (Physica Scripta/The Royal Academy of Sciences/World Scientific, Singapore, 2003).

[57] E. Fradkin, A. Auerbach. "Interacting Electrons and Quantum Magnetism." (1994)

[58] A. Eckardt, C. Weiss, et al. "Superfluid-insulator transition in a periodically driven optical lattice." Physical review letters 95.26 (2005): 260404.

[59] N. F. Mott, "Metal-insulator transition." Reviews of Modern Physics 40.4 (1968): 677.

[60] Anderson, Philip W. "Absence of diffusion in certain random lattices." Physical review 109.5 (1958): 1492.

[61] R. Roth, K. Burnett. "Ultracold bosonic atoms in two-colour superlattices." Journal of Optics B: Quantum and Semiclassical Optics 5.2 (2003): S50.

[62] Damski, Bogdan, et al. "Atomic Bose and Anderson glasses in optical lattices." Physical review letters 91.8 (2003): 080403.

[63] A. Sanpera, et al. "Atomic Fermi-Bose mixtures in inhomogeneous and random lattices: From Fermi glass to quantum spin glass and quantum percolation." Physical review letters 93.4 (2004): 040401.

[64] V. Ahufinger, et al.""Disordered ultracold atomic gases in optical lattices: A case study of Fermi-Bose mixtures." Physical Review A 72.6 (2005): 063616.

[65] A. Honecker, et al. “Finite-temperature ordering in a two-dimensional highly frustrated spin model.” Journal of Physics: Condensed Matter 19.14 (2007): 145249.

[66] J. Wehr, et al. “Disorder versus the Mermin-Wagner-Hohenberg effect: From classical spin systems to ultracold atomic gases.” Physical Review B 74.22 (2006): 224448.

[67] U. Dorner, et al. “Entangling strings of neutral atoms in 1D atomic pipeline structures.” Physical review letters 91.7 (2003): 073601.

[68] Douçot, Benoît, et al. ”Protected qubits and Chern-Simons theories in Josephson junction arrays.” Physical Review B 71.2 (2005): 024505.

[69] L.-M. Duan, E. Demler, and M. D. Lukin. ”Controlling spin exchange interactions of ultracold atoms in optical lattices.” Physical review letters 91.9 (2003): 090402.

[70] A. Micheli, G. K. Brennen, and P. Zoller. “A toolbox for lattice-spin models with polar molecules.” Nature Physics 2.5 (2006): 341.

[71] Moses, Steven A., et al. “Creation of a low-entropy quantum gas of polar molecules in an optical lattice.” Science 350.6261 (2015): 659-662.

[72] W. Demtröder, “Experimentalphysik 3: Atome, Moleküle und Festkörper” Springer Verlag (2000)

[73] A. Ashkin, and J.M. Dziedzic. “Optical trapping and manipulation of viruses and bacteria.” Science 235.4795 (1987): 1517-1520.

[74] T. A. Savard, K. M. O’Hara, et al. “Laser-noise-induced heating in far-off resonance optical traps.” Physical Review A 56.2 (1997): R1095.

[75] M. E. Gehm, K. M. O’Hara, et al. “Dynamics of noise-induced heating in atom traps,” Physical Review A 58.5 (1998): 3914.

[76] M. Gustavsson, “A quantum gas with tuneable interactions in an optical lattice,” PhD thesis, University of Innsbruck (2008)

[77] O. Morsch, M. Oberthaler. “Dynamics of Bose-Einstein condensates in optical lattices.” Reviews of modern physics 78.1 (2006): 179.

[78] I. Bloch, J.Dalibard, and W. Zwerger. “Many-body physics with ultracold gases.” Reviews of modern physics 80.3 (2008): 885.

[79] M. Zwerger, “Mott–Hubbard transition of cold atoms in optical lattices.” Journal of Optics B: Quantum and Semiclassical Optics 5.2 (2003): S9.

[80] https://www.thorlabs.de/newgrouppage9.cfm?objectgroup_id=266&pn=NE40A (11.10.18)

[81] https://picamera.readthedocs.io/en/release-1.13/fov.html (23.10.18)

[82] William M. Haynes, “CRC Hnadbook of Chemistry and Physics: a ready-reference Book of chemical and physical data,” RCR Press (2011)

[83] http://www.allanstime.com/Publications/DWA/Conversion_from_Allan_variance_to_Spectral_Densities.pdf (30.01.18)

[84] D. A. Steck, “Rubidium 87 D Line Data” (2015)

[85] NKT Koheras Boostik laser datasheet https://www.nktphotonics.com/wp-content/uploads/sites/3/2015/03/koheras-boostik.pdf?1539441747 (12.10.18)

[86] datasheet of the Sony IMX219PQ CMOS-chip https://www.sony-semicon.co.jp/products_en/new_pro/april_2014/imx219_e.html (12.10.18)

[87] Laura Corman, “The two-dimensional Bose Gas in box potentials,” Physics [physics]. PSL Research University, 2016. English. <NNT: 2016PSLEE014>

[88] Ville, J. L., et al. “Loading and compression of a single two-dimensional Bose gas in an optical accordion.” Physical Review A 95.1 (2017): 013632.

[89] S. Hammer, “Setting up a lightsheet for realizing quasi two-dimensional quantum gases,” Bachelor thesis, University of Stuttgart (2017)

[90] L. C. Li, H. Kelkar et al. “Real-time control of the periodicity of a standing wave: an optical accordion,” Optics express 16.8 (2008): 5465-5470.

[91] Luca Schmidt, “Setting up an accordion lattice to determine the resolution of a Rydberg ion imaging system” B.Sc. thesis, University of Stuttgart (2018)

[92] R. A. Williams, et al. ”Dynamic optical lattices: two-dimensional rotating and accordion lattices for ultracold atoms.Öptics Express 16.21 (2008): 16977-16983.

[93] Hannes M. Gorniaczyk “A Crossed Optical Dipole Trap,” Diploma thesis, University of Stuttgart (2011)

[94] Jonathan B. Balewski, “A single electron in a Bose-Einstein condensate,” PhD thesis. University of Stuttgart (2014)